



# Search for New Physics in All-hadronic Events with AlphaT in 8 TeV data at CERN

Yossof Eshaq

*Submitted in Partial Fulfillment of the  
Requirements for the Degree Doctor of Philosophy*

Supervised by Professor Aran Garcia-Bellido

Department of Physics

Astronomy

Arts, Sciences and Engineering

University of Rochester

October 3, 2014

## Abstract

An inclusive search for supersymmetric processes that produce final states with jets and missing transverse energy is performed in pp collisions at a centre-of-mass energy of  $\sqrt{s} = 8$  TeV. The data sample corresponds to an integrated luminosity of  $18.5 \text{ fb}^{-1}$  collected by the CMS experiment at the LHC. In this search, a dimensionless kinematic variable,  $\alpha_T$ , is used to discriminate between events with genuine and misreconstructed missing transverse energy. The search is based on an examination of the number of reconstructed jets per event, the scalar sum of transverse energies of these jets, and the number of these jets identified as originating from bottom quarks. The results are interpreted with various simplified models, with a special emphasis on models with a compressed mass spectrum.

## 1 Theoretical motivation

SM,Higgs,SUSY

Particle physics concerns itself with the study of particles and fields. Our current knowledge of their characteristics and interactions are formalized in the quantum field theory called the Standard Model. It through three symmetries: The color charge symmetry of Quantum Chromo Dynamics (QCD) represented in  $SU(3)$ , the flavor symmetry of Quantum Flavor Dynamics (QFD) represented in  $SU(2)$  and the electric charge symmetry of Quantum Electro Dynamics represented in  $U(1)$ . Together,  $SU(3) \times SU(2) \times U(1)$  represent the field theory.

## **2 LHC and CMS**

LHC, CMS

### **3 Definition of $\alpha_T$**

## 4 Data sets and Monte Carlo samples

### 4.1 Data sets

The data analysed consist of the full run of 2012.

The following datasets are used to populate the hadronic signal and control samples. They correspond to the full data run of 2012 and an integrated luminosity of  $19.45 \pm 0.8 \text{ fb}^{-1}$ . The official JSON from the 22<sup>nd</sup> Jan 2013 is used to filter only certified luminosity sections with the run range 190456–208686.

Table 1: Datasets.

Dataset	Luminosity ( $\text{fb}^{-1}$ )
Hadronic	19.45
Muon	19.72
Photon	19.63

### 4.2 MC samples for signal and SM backgrounds

The SM background Monte Carlo samples for physics at 8 TeV are taken from the Summer12 simulation production run with CMSSW\_5\_3\_X with the PU\_S10 scenario. The effective luminosity of each MC sample is normalised to the integrated luminosity of the corresponding dataset, as listed in Table 2. The signal MADGRAPH Monte Carlo samples, listed in Table ??, are taken from a FastSim simulation production based on CMSSW\_5\_2\_X. All MC samples are reweighted on an event-by-event basis such that the distribution of pile-up (PU) interactions matches that observed in data. This is done using the recommended recipe and the PU JSON of 13<sup>th</sup> December 2012.

Table 2: MC samples for Standard Model processes.

Sample	HT (GeV)	Cross section (pb)	Corrected Cross section (pb)
$W \rightarrow l\nu$	Inclusive	37509.0	34133.2
$W \rightarrow l\nu$	150 - 200	253.8	234.53
$W \rightarrow l\nu$	200 - 250	116.5	103.94
$W \rightarrow l\nu$	250 - 300	57.6	51.34
$W \rightarrow l\nu$	300 - 400	48.4	42.41
$W \rightarrow l\nu$	400 - $\infty$	30.8	26.36
$Z \rightarrow \nu\bar{\nu}$	50 - 100	452.8	405.21
$Z \rightarrow \nu\bar{\nu}$	100 - 200	190.4	173.76
$Z \rightarrow \nu\bar{\nu}$	200 - 400	45.1	42.41
$Z \rightarrow \nu\bar{\nu}$	400 - $\infty$	6.26	5.81
$t\bar{t}$	Inclusive	234.0	271.44
$Z/\gamma^* \rightarrow l^+l^- (m_{ll} > 50)$	Inclusive	3503.7	3258.45
$Z/\gamma^* \rightarrow l^+l^- (10 < m_{ll} < 50)$	Inclusive	13124.1	12205.4
$Z/\gamma^* \rightarrow l^+l^-$	200 - 400	24.3	22.24
$Z/\gamma^* \rightarrow l^+l^-$	400 - $\infty$	3.36	3.11
$\gamma + \text{jets}$	200 - 400	1140.8	1060.9
$\gamma + \text{jets}$	400 - $\infty$	124.7	115.97
WW	Inclusive	57.1	57.1
WZ	Inclusive	12.6	12.6
ZZ	Inclusive	8.26	8.26
$t$ (t-channel)	Inclusive	56.4	56.4
$\bar{t}$ (t-channel)	Inclusive	30.7	30.7
$t$ (s-channel)	Inclusive	3.79	3.79
$\bar{t}$ (s-channel)	Inclusive	1.76	1.76
$t$ (tW-channel)	Inclusive	11.1	11.1
$\bar{t}$ (tW-channel)	Inclusive	11.1	11.1

### 4.3 Corrections to cross sections for SM samples

A simulated event is weighted by the total number of events in the MC sample, the theoretical cross section, and total luminosity of the data being studied. The MC POG provides next-to-next-to leading order (NNLO) theoretical cross section for un-filtered (inclusive) SM samples [7]. In an attempt to provide higher statistics in tails of distribution analyses often cut on (ie  $H_T^{\text{parton}}$ ,  $N^{\text{parton}}$ ,  $\hat{p}_T$ ), MC samples are provided binned in these variables. Only the leading-order (LO) cross sections are provided [6] but in general, the  $k$ -factors required to go from LO to NNLO cross sections are determined using corresponding inclusive samples and applied to each binned sample.

Studies conducted by other analyses [11] revealed that some LO cross sections calculated for MC samples binned according to  $H_T^{\text{parton}}$  are inaccurate to a level as large as 10%, leading to non-physical discontinuities in the  $H_T^{\text{parton}}$  distribution constructed from the binned samples of a



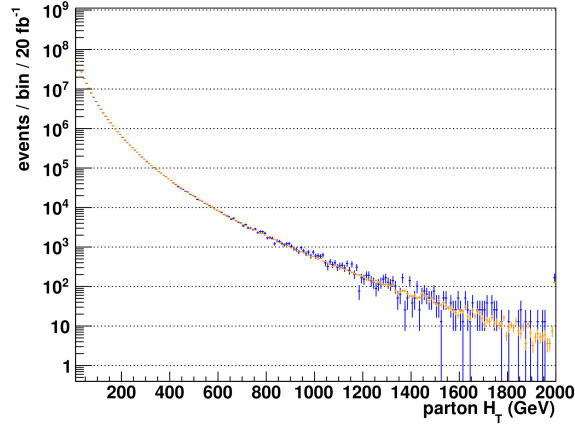
given process. Furthermore, due to an error in production, the  $W \rightarrow l\nu$   $H_T$  binned samples exhibit  $H_T$ -dependent biases. The following paragraphs describes a procedure to measure corrections to the discontinuities and biases of the  $W \rightarrow l\nu$   $H_T^{\text{parton}}$  binned samples as a function of  $H_T$ . Other analyses created similar procedures to correct the  $Z \rightarrow \mu\mu$   $H_T^{\text{parton}}$  binned samples, this analysis uses those measured corrections as k-factors.

As a first step, we wish to reweigh the cross sections of the  $H_T^{\text{parton}}$  binned samples such that their  $H_T^{\text{parton}}$  distributions match that of the inclusive sample's. Due to the inclusive sample's limited statistics in the tails of  $H_T$  distribution, we instead use the  $N^{\text{parton}}$  binned's  $H_T^{\text{parton}}$  distribution which is verified to agree well with the inclusive sample figure 1 (a). Additionally, to smooth statistical fluctuations, both distributions are fitted using a double exponential of the form  $\exp(a + b * x + c * x^{1.05})$  for  $H_T > 500$  GeV figure 1 (b). The ratio of the distributions figure 1(c) is applied as  $H_T^{\text{parton}}$  dependent event weight.

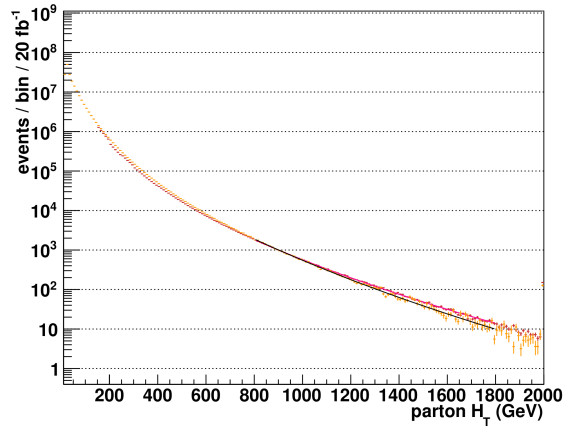
In the high- $H_T$  and high- $E_T$  corner of kinematic phase space of this analysis (and other SUSY analyses) the overall normalization of MC samples do not agree well with data. Therefore a data sideband in  $H_T$  is used to determine sample-specific corrections that are appropriate for the  $H_T$ - $E_T$  phase space covered by this analysis. This correction is determined for the  $W \rightarrow l\nu$  and  $t\bar{t}$  samples by imposing requirements on the number of muons, jets, and b-tagged jets, to obtain samples rich in  $W$  + jets, and  $t\bar{t}$  events. A sideband in  $H_T$  is used to determine both the yields in data and MC expectations. The sideband is defined by the region  $200 < H_T < 225$  GeV and uses the jet  $p_T$  thresholds (73, 73, 37 GeV) to maintain comparable jet multiplicities, kinematics, and background admixtures as observed for the higher HT bins. Trigger efficiency and b-tag scale factor corrections are determined and applied to the MC samples. The purity of the samples are  $> 80\%$  and any contamination is taken into account. The correction is determined by taking the ratio of the data yield over the MC expectation in the sideband. Table 3 summarises the selection and corrections for the different samples.

Table 3: Correctins determined from a data sideband for the W + jets and  $t\bar{t}$  samples. “Corrected yield” reflects the observed data yield minus the contamination as given by MC.

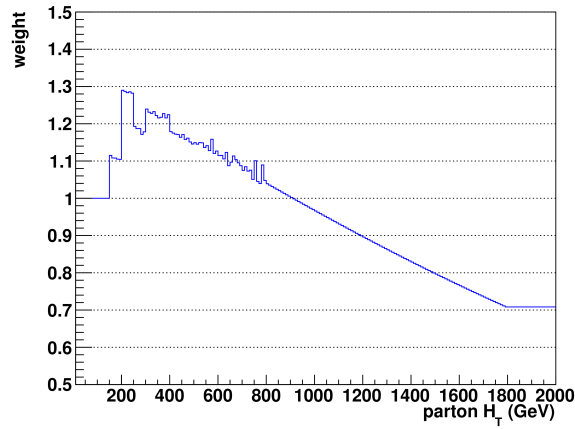
Process	Selection	Purity	Corrected yield	MC expectation	Correction Factor
W + jets	$\mu + \text{jets}, 2 \leq n_{\text{jet}} \leq 3, n_b = 0$	0.90	15682	$18013.1 \pm 85.9$	$0.87 \pm 0.01$
$t\bar{t}$	$\mu + \text{jets}, n_{\text{jet}} \geq 2, n_b \geq 2$	0.83	752	$736.7 \pm 11.5$	$1.02 \pm 0.05$



(a) Parton  $H_T$  distribution for the  $W \rightarrow l\nu$  inclusive sample (blue) and  $W \rightarrow l\nu N^{\text{parton}}$  binned sample (orange.)



(b) Fitted Parton  $H_T$  distribution for the  $W \rightarrow l\nu H_T^{\text{parton}}$  sample (purple) and  $W \rightarrow l\nu N^{\text{parton}}$  binned sample (orange.)



(c) Event weight determined from ration of figure 1 (b)

Figure 1: Generator-level  $H_T^{\text{parton}}$  distributions and measured weights

## 5 Hadronic Event Selection

As discussed in [REF], all-hadronic SUSY signatures consist of events with no isolated and detectable objects apart from energetic jets. To search for an excess in such events, it is convenient to use a jet-based variable,  $H_T$ , to quantify the energy in an event.  $H_T$  is defined as the scalar sum of the transverse energy of the jets in the event. The challenges due to large backgrounds in a search for an excess in all-hadronic events becomes evident when comparing observed data events overlaid with simulated events from SM processes as a function of  $H_T$  Figure [REF].

The dominant background are azimuthally-balanced multi-jet events, stemming from QCD processes. This search reduces this background to negligible levels in the selected region by employing the  $\alpha_T$  variable further discussed in section [REF]. Furthermore, by construction,  $\alpha_T$  also reduces backgrounds from severely mis-measured jets.

In absence of the multi-jet background, the remaining significant backgrounds are ...

### 5.1 Data

The data analyzed was recorded by CMS in 2012 between April 5th and Dec. 5th and totals  $19.47 \pm 2.6\%$ . The collected data is certified on a run-by-run basis, where initial automatic certification requires the LHC beams to be declared stable and all CMS subdetectors ON. Further monitoring of the data was done realtime by experts of each subdetector through analysis of histograms updated and filled each lumi section. Final certification was done offline, and lumi sections passing all criteria were listed in a Golden JSON file to be used by all analyses.

### 5.2 Event quality

Each event is subjected to a series of commonly used filters in CMS to ensure good quality data. Minimal requirements are that at least one primary vertex is identified and 25% of the reconstructed tracks to be of good quality. Additionally, various filters prescribed by the MET group[REF] are

applied. Events containing muons with inconsistent energy are flagged by the muon pog [REF] and filtered out of the analysis.

### 5.3 Triggers

#### 5.3.1 Hadronic signal region and control samples

Only events passing one or more HLT triggers based on online quantities are recorded to be analyzed. For any analysis, in general, it is not expected that all recorded events reconstructed offline, pass the online trigger as detector conditions, energy corrections, and object-based quantities differ offline. In this analysis, cross-triggers at the HLT based on quantities  $H_T$  and  $\alpha_T$  (labelled as HTxxx\_AlphaT0pyy) are used with various thresholds to record candidate events for the hadronic (signal) region. In order to keep the cross-trigger's computational time low, the online quantities are constructed using simple calorimeter based jets (calo jets), and the use of particle-flow jets in this analysis is expected to introduce inefficiencies.

Each  $H_T$  bin is seeded by a single trigger chosen based on the efficiency of the trigger in that  $H_T$  bin. The  $\alpha_T$  thresholds of the HTxxx\_AlphaT0pyy triggers were tuned according to the threshold on the  $H_T$  leg in order to fully suppress QCD multijet events and simultaneously satisfying other criteria, such as maintaining acceptable trigger rates.

The HTxxx\_AlphaT0pyy trigger efficiencies are measured with a reference (i.e., unbiased) event sample recorded by an unprescaled, loosely-isolated, eta-restricted single muon trigger, HLT\_IsoMu24\_eta2p1, within the SingleMu dataset. A sample of events containing at least one isolated muon with  $p_T > 25 \text{ GeV}$  and  $|\eta| < 2.1$  is used (similar to the  $\mu + \text{jets}$  control sample defined in Section ??). A cut of  $\Delta R > 0.5$  is placed between all muons and jets in each event, and only jets are considered in the calculation of  $H_T$ ,  $H_T$ , and  $\alpha_T$ , i.e. the muon is ignored.

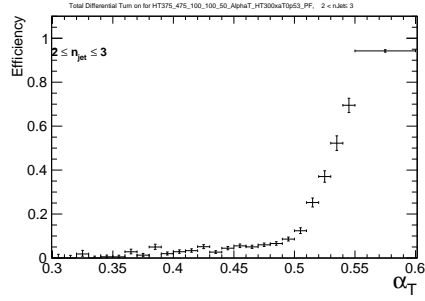
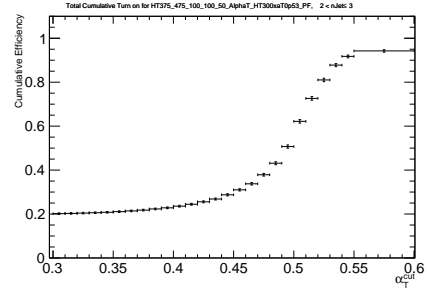
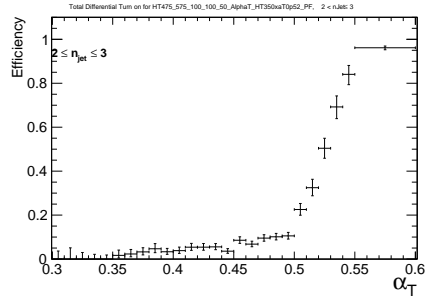
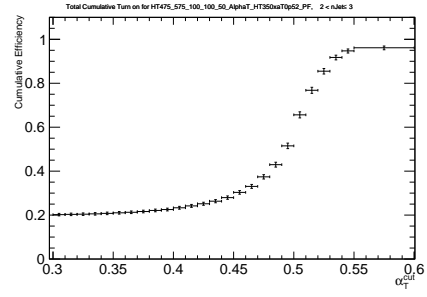
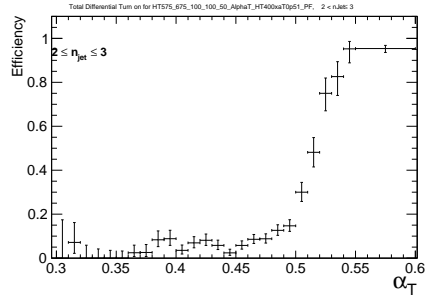
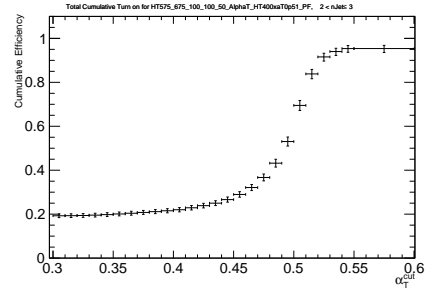
(a) Differential,  $375 < H_T < 475$  GeV(b) Cumulative,  $375 < H_T < 475$  GeV(c) Differential,  $475 < H_T < 525$  GeV(d) Cumulative,  $475 < H_T < 525$  GeV(e) Differential,  $525 < H_T < 675$  GeV(f) Cumulative,  $525 < H_T < 675$  GeV

Figure 2: (Left) Differential and (Right) cumulative efficiency turn-on curves for the  $H_T$ - $\alpha_T$  cross triggers (as summarised in Table ??) that record events for the three lowest  $H_T$  bins for events satisfying  $2 \leq n_{\text{jet}} \leq 3$ .

### 5.3.2 Muon control samples

## 5.4 event selection

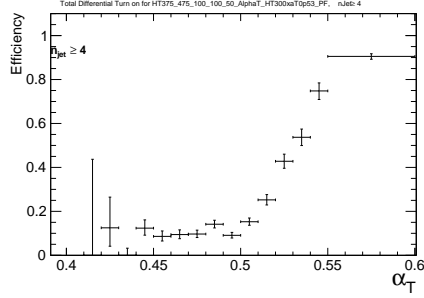
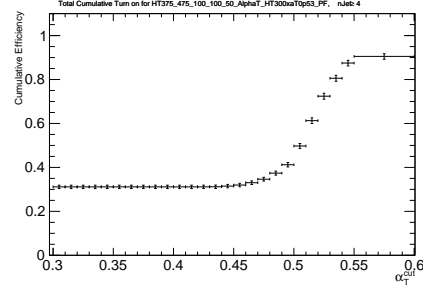
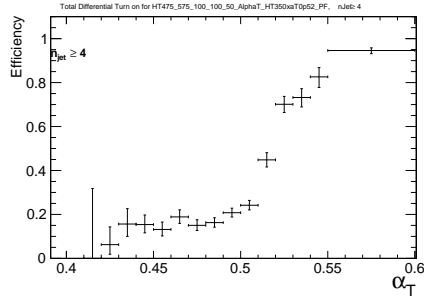
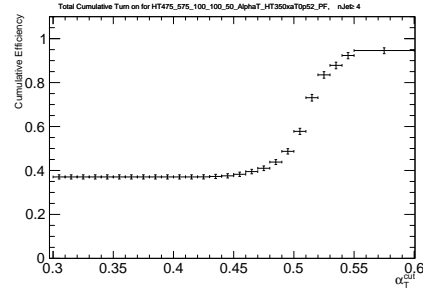
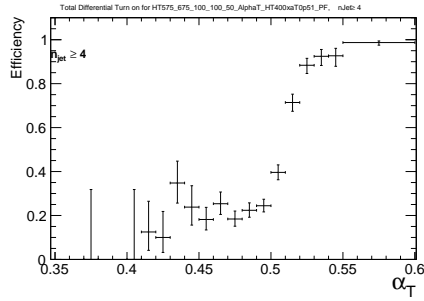
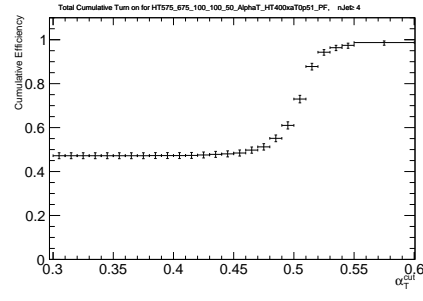
(a) Differential,  $375 < H_T < 475$  GeV(b) Cumulative,  $375 < H_T < 475$  GeV(c) Differential,  $475 < H_T < 525$  GeV(d) Cumulative,  $475 < H_T < 525$  GeV(e) Differential,  $525 < H_T < 675$  GeV(f) Cumulative,  $525 < H_T < 675$  GeV

Figure 3: (Left) Differential and (Right) cumulative efficiency turn-on curves for the  $H_T$ - $\alpha_T$  cross triggers (as summarised in Table ??) that record events for the three lowest  $H_T$  bins for events satisfying  $n_{\text{jet}} \geq 4$ .

## 6 Closure tests and systematic uncertainties on transfer factors

Limitations in simulating detector effects and event kinematics requires us to apply appropriate systematic uncertainties on the simulation-based translation factors. The following section describes how we obtain these uncertainties through the method of closure tests.

### 6.1 Closure tests

At its core, the method compares an observed yield ( $N_{\text{obs}}$ ) and a predicted yield ( $N_{\text{pred}}$ ) in a subsample of a control region. The predicted yield is constructed by translating from a statistically independent data sample to the data sample of interest by the use of the proper translation factor. For example, in a given  $H_T$  bin, a prediction for the  $n_{\text{jet}} \geq 4$ ,  $n_b = 1$ ,  $\mu + \text{jets}$  sample can be made by translating from the  $2 \leq n_{\text{jet}} \leq 3$ ,  $n_b = 1$ ,  $\mu + \text{jets}$  in data via the translation factor:

$$\frac{N_{\text{MC}}^{\mu+\text{jets}}(H_T, n_{\text{jet}} \geq 4, n_b = 1)}{N_{\text{MC}}^{\mu+\text{jets}}(H_T, 2 \leq n_{\text{jet}} \leq 3, n_b = 1)} \quad (1)$$

The agreement between  $N_{\text{obs}}$  and  $N_{\text{pred}}$  is expressed as  $(N_{\text{obs}} - N_{\text{pred}})/N_{\text{pred}}$ . Assuming only statistical uncertainties on  $N_{\text{obs}}$  and  $N_{\text{pred}}$ , deviation of the ratio from zero defines our level of closure. A closure test set is defined as ratios for each  $H_T$  bin. Looking at the ratio as a function of  $H_T$  allows the measurement of statistical significant biases from zero and/or any dependence on  $H_T$ . If statistically significant biases are observed, further studies are required to understand and correct for these biases.

Eight sets of closure tests probe key ingredients of the simulation modeling of the SM backgrounds with genuine  $E_T$  as a function of  $H_T$ , as shown in Fig. 4. This is done for the two jet multiplicity bins separately: (a)  $2 \leq n_{\text{jet}} \leq 3$  and (b)  $n_{\text{jet}} \geq 4$ .

Under the assumption of closure for the full ensemble of tests, systematic uncertainties on the transfer factors are derived for each  $n_{\text{jet}}$  category and  $H_T$  regions. The treatment for estimating the



systematic uncertainties on the transfer factors is described in Section 6.2.

As described in section ?? The  $\alpha_T$  requirement is not imposed in the  $\mu$  + jets control sample. Therefore it is important to verify the approach of using  $\mu$  + jets samples without an  $\alpha_T$  requirement to make background predictions in the signal region. The first set of closure tests (denoted by circles) attempts to do this by probing the modeling of the  $\alpha_T$  distribution in genuine  $E_T$  events as a function of  $H_T$ . The tests compares data yields in the  $\mu$  + jets sample with an  $\alpha_T$  requirement against predictions determined in a  $\mu$  + jets sample with the  $\alpha_T$  requirement inverted.

The next three sets (triangles, crosses, squares) probe the sensitivity of the transfer factors to the relative admixture of events from the  $W$  + jets and  $t\bar{t}$  processes. These tests are conservative, since by construction, the admixture changes little when translating from the  $\mu$  + jets control region to the signal region, whereas the closure tests use sub-samples with different b-tag requirements and therefore have very different admixtures of  $W$  + jets and  $t\bar{t}$  events. In the  $2 \leq n_{\text{jet}} \leq 3$  bin, the test is sub-divided into separate jet categories. These tests also probe the modeling of the reconstruction of b-quark jets, although this also addressed more fully by dedicated studies that determine systematic uncertainties via the method described in Sec. ??.

The remaining tests probe the simulation modeling of the jet multiplicity in the  $\mu$  + jets and  $\gamma$  + jets samples, which is checked due to the exclusive binning in jet multiplicity. As in the case of the  $W$  + jets /  $t\bar{t}$  admixture, this set of tests is a very conservative check, as predictions are always made from the same jet multiplicity bin, whereas the closure tests translate between the two bins.

Tables 4 and 5, which summarize the results obtained from fits of zeroth order polynomials (i.e. a constant) to the sets of closure tests performed in the  $2 \leq n_{\text{jet}} \leq 3$  and  $n_{\text{jet}} \geq 4$  bins. Table 6 lists the fits result common to both jet multiplicities. The best fit value and its uncertainty is listed for each set of closure tests, along with the  $\chi^2$ , the number of degrees of freedom, and the p-value of the fit. The best fit value for the constant parameter is indicative of the level of closure, as averaged across the full  $H_T$  range considered in the analysis, and the p-value is indicative of whether there

is any significant dependence on  $H_T$ .

The closure tests demonstrate, within the statistical precision of each test, that there are no significant biases or dependencies on  $H_T$  inherent in the transfer factors obtained from simulation.

One set of tests does indicate a poor goodness of fit (indicated by a low  $p$ -value), which is the  $n_b = 0 \rightarrow n_b = 1$  test in the  $\mu + \text{jets}$  sample for the  $n_{\text{jet}} \geq 4$  category, which has been identified as a upward (downward) fluctuation of event counts in the  $H_T$  bin 475–575 GeV (575–675 GeV) when  $n_b = 1$ . Combining these two bins yields an acceptable fit result, as indicated in Table 5, which points to a simple fluctuation rather than any systematic bias.

Table 4: A summary of the results obtained from fits of zeroth order polynomials (i.e. a constant) to four sets of closure tests performed in the  $2 \leq n_{\text{jet}} \leq 3$  bin.

Closure test	Symbol	Constant fit			
		Best fit value	$\chi^2$	d.o.f.	$p$ -value
$\alpha_T < 0.55 \rightarrow \alpha_T > 0.55$ ( $\mu + \text{jets}$ )	Circle	$0.007 \pm 0.02$	3.91	7	0.79
1 b-tags $\rightarrow$ 2 b-tags ( $\mu + \text{jets}$ , nJet=3)	Triangle	$-0.008 \pm 0.04$	3.20	7	0.87
0 b-tags $\rightarrow$ 1 b-tags ( $\mu + \text{jets}$ , nJet=2)	Cross	$0.111 \pm 0.03$	5.87	7	0.55
0 b-tags $\rightarrow$ 1 b-tags ( $\mu + \text{jets}$ , nJet=3)	Square	$0.040 \pm 0.02$	1.12	7	0.99

Table 5: A summary of the results obtained from fits of zeroth order polynomials (i.e. a constant) to three sets of closure tests performed in the  $n_{\text{jet}} \geq 4$  bin. <sup>†</sup>Further explanation of this fit can be found in the text.

Closure test	Symbol	Constant fit			
		Best fit value	$\chi^2$	d.o.f.	$p$ -value
$\alpha_T < 0.55 \rightarrow \alpha_T > 0.55$ ( $\mu + \text{jets}$ )	Circle	$0.011 \pm 0.04$	5.81	7	0.56
1 b-tags $\rightarrow$ 2 b-tags ( $\mu + \text{jets}$ )	Triangle	$0.045 \pm 0.03$	9.36	7	0.23
0 b-tags $\rightarrow$ 1 b-tags ( $\mu + \text{jets}$ )	Square	$0.007 \pm 0.03$	25.30	7	0.00
0 b-tags $\rightarrow$ 1 b-tags ( $\mu + \text{jets}$ ) <sup>†</sup>	Square	$0.009 \pm 0.03$	10.12	6	0.12

Table 6: A summary of the results obtained from fits of zeroth order polynomials (i.e. a constant) to four sets of closure tests ( $2 \leq n_{\text{jet}} \leq 3 \rightarrow n_{\text{jet}} \geq 4$ ) that probe the accuracy of the MC modeling of the  $n_{\text{jet}}$  distribution observed in data, using the three data control samples.

Closure test	Symbol	Constant fit			
		Best fit value	$\chi^2$	d.o.f.	$p$ -value
$2 \leq n_{\text{jet}} \leq 3 \rightarrow n_{\text{jet}} \geq 4$ ( $\mu$ + jets, 1 b-tags)	Times	$-0.053 \pm 0.03$	8.02	7	0.33
$2 \leq n_{\text{jet}} \leq 3 \rightarrow n_{\text{jet}} \geq 4$ ( $\mu$ + jets, 1 b-tags)	Invert. Triangle	$0.018 \pm 0.04$	6.23	7	0.51
$2 \leq n_{\text{jet}} \leq 3 \rightarrow n_{\text{jet}} \geq 4$ ( $\mu$ + jets, 0 b-tags)	Star	$0.034 \pm 0.02$	9.24	7	0.24
$2 \leq n_{\text{jet}} \leq 3 \rightarrow n_{\text{jet}} \geq 4$ ( $\gamma$ + jets, 0 b-tags)	Diamond	$0.100 \pm 0.04$	12.20	7	0.09

## 6.2 Systematic uncertainties from closure tests

Once it is established that no significantly large bias or trend is observed for any set of closure tests, then systematic uncertainties are determined.

Systematics uncertainties are determined for each  $H_T$  bin, as indicated in Table 7. For each  $H_T$  region, the systematic uncertainty is estimated by taking the quadrature sum of the weighted mean and sample variance for the closure tests within the given  $H_T$  region. This procedure yields the values quoted in Table 7.

As the closure tests do not translate from control region to signal region, they do not probe the uncertainty in the signal trigger efficiencies. To account for this, a trigger uncertainty of 5% is added in quadrature to the uncertainty values obtained via the closure tests and the total is summarized in Table 8.

Table 7: A summary of the magnitude of the systematic uncertainties (%) obtain from closure tests, according to  $n_{\text{jet}}$  and  $H_T$  region.

$n_{\text{jet}}$	$H_T$ region (GeV)							
	375–475	475–525	525–675	675–775	775–875	875–975	1075–1075	> 1175
2–3	3	4	5	11	11	16	16	16
$\geq 4$	3	4	6	13	13	13	13	20

Figure 4 shows the sets of closure tests overlaid on top of gray bands that represent the  $H_T$ -

Table 8: A summary of the magnitude of the total systematic uncertainties (%) assigned to the transfer factors, according to  $n_{\text{jet}}$  and  $H_{\text{T}}$  region.

$n_{\text{jet}}$	$H_{\text{T}}$ region (GeV)							
	375–475	475–525	525–675	675–775	775–875	875–975	1075–1075	> 1175
2–3	6	6	7	12	12	17	17	17
$\geq 4$	6	6	8	14	14	14	14	21

dependent systematic uncertainties in Table 7. These systematic uncertainties are assumed to fully uncorrelated between the different b jet multiplicity categories and also the eight  $H_{\text{T}}$  regions, which is a conservative approach given that one can expect some correlation between adjacent  $H_{\text{T}}$  bins (due to comparable kinematics).

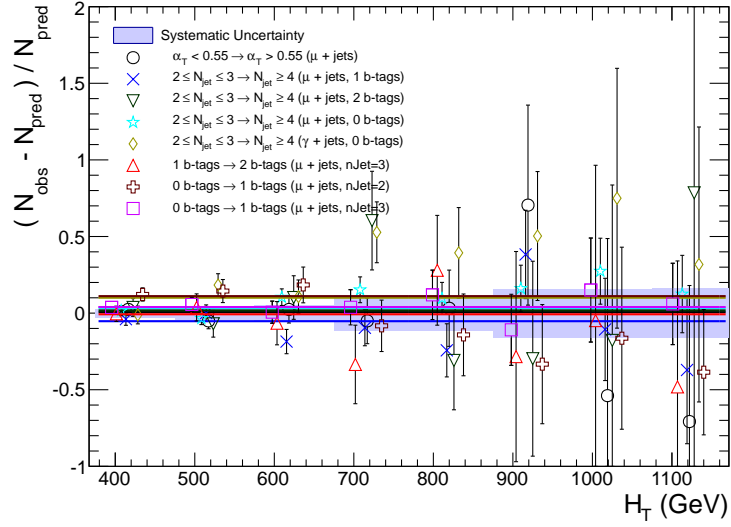
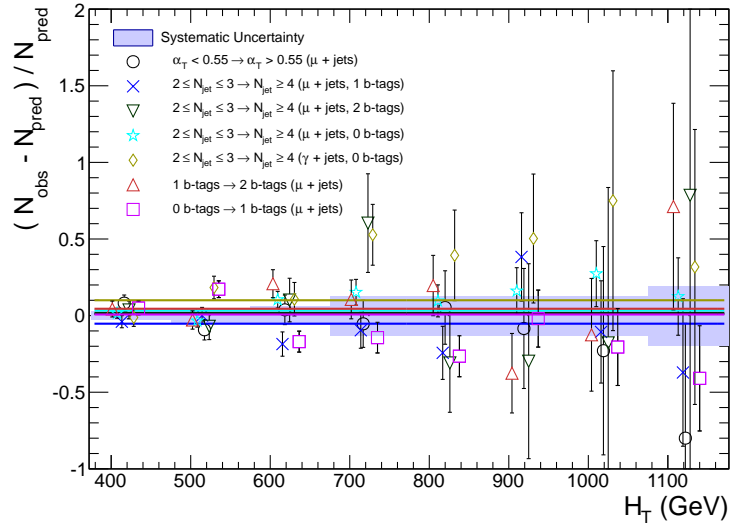
(a)  $2 \leq n_{\text{jet}} \leq 3$ (b)  $n_{\text{jet}} \geq 4$ 

Figure 4: Sets of closure tests (open symbols) overlaid on top of the systematic uncertainty used for each of the  $H_T$  region (shaded bands) and for the two different jet multiplicity bins: (a)  $2 \leq n_{\text{jet}} \leq 3$  and (b)  $n_{\text{jet}} \geq 4$ .

## 7 Results

The likelihood described in ref:likelihood is used to relate yields, uncertainties. It is constructed using ROOTFIT [12] and maximized using MINUIT [9].

### 7.1 Standard Model

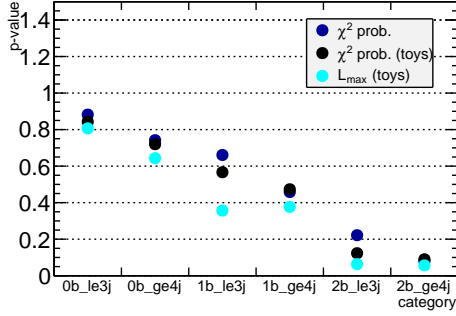
To test compatibility with a Standard Model only hypothesis, the signal term is removed from the likelihood model. The parameter values maximizing the likelihood function are listed in Tables 15–20 found in Appendix A. The resulting SM yields along with the observed data yields are summarized in Tables B. The uncertainty on the yields are obtained by constructing a probability density function (p.d.f) from the maximized likelihood, then generating an ensemble of pseudo-experiments from this p.d.f. and maximizing the same likelihood form for each pseudo-experiment, resulting in an ensemble of yields. The 68% quantile of each ensemble defines the quoted uncertainty on the corresponding yield.

Figures 6–11 show the  $H_T$ -binned observed data yields (black filled circles) and the SM expectations and uncertainties (dark blue solid line with light blue bands) as determined by the fit for the hadronic signal region and the  $\mu + \text{jets}$  or both ( $\mu + \text{jets}, \gamma + \text{jets}$ ) control samples, depending on the event category. The uncertainties in the SM expectations obtained from the ensemble of pseudo-experiments reflect the statistical uncertainties in the considered data samples and the systematic uncertainties in the transfer factors as discussed in section 6. Figures 6–11 are summarized in tabular format in Tables 21–26 in appendix B along with observed data yields and the fit result for all event categories and both signal region and control sample bins.

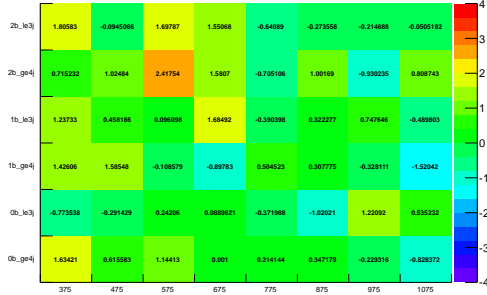
For each  $n_b, n_{\text{jet}}$  category, the goodness-of-fit of the SM-only hypothesis is determined by considering simultaneously all  $H_T$  bins entering the likelihood. The goodness-of-fit described in [8] is obtained by comparing the nominal maximized likelihood value  $L_{\text{max}}^{\text{data}}$  to the corresponding ensemble of values,  $L_{\text{max}}$ . The quantile which  $L_{\text{max}}^{\text{data}}$  falls in the distributions is interpreted as a

p-value. A p-value derived from a chi-square is also plotted for comparison.

The p-values obtained, shown in Figure 5 (Left), are found to be uniformly distributed in the range 0.0–1.0, with the lowest p-value determined to be 0.17.



(a) p-values per event category.



(b) Pull versus signal region bin.

Figure 5: Pulls and p-values. See text for details

Table 9: Summary of hadronic yields from fit.

	375–475	475–575	575–675	675–775	775–875	875–975	975–1075	1075–∞
0b le3j SM	$2744^{+48}_{-43}$	$771^{+21}_{-23}$	$254^{+13}_{-13}$	$76.5^{+6.1}_{-4.8}$	$33.7^{+3.7}_{-3.8}$	$11.8^{+1.9}_{-2.1}$	$6.3^{+1.4}_{-1.3}$	$3.2^{+1.0}_{-0.9}$
0b le3j Data	2728	766	257	77	32	9	9	4
1b le3j SM	$426^{+15}_{-17}$	$114^{+6}_{-6}$	$35.5^{+3.3}_{-2.8}$	$10.1^{+1.4}_{-1.5}$	$3.7^{+0.9}_{-0.8}$	$1.6^{+0.7}_{-0.6}$	$0.5^{+0.3}_{-0.4}$	$0.1^{+0.1}_{-0.0}$
1b le3j Data	444	118	36	15	3	2	1	0
2b le3j SM	$65.0^{+4.3}_{-4.3}$	$18.4^{+1.7}_{-1.6}$	$4.2^{+0.6}_{-0.5}$	$1.1^{+0.3}_{-0.2}$	$0.2^{+0.1}_{-0.1}$	$0.0^{+0.0}_{-0.0}$	$0.0^{+0.0}_{-0.0}$	$0.0^{+0.0}_{-0.0}$
2b le3j Data	78	18	8	3	0	0	0	0
0b ge4j SM	$456^{+15}_{-14}$	$291^{+12}_{-12}$	$148^{+8}_{-7}$	$66.0^{+5.6}_{-5.2}$	$27.1^{+2.9}_{-3.4}$	$14.0^{+1.9}_{-2.1}$	$6.5^{+1.5}_{-1.2}$	$3.2^{+1.0}_{-0.9}$
0b ge4j Data	480	299	158	66	28	15	6	2
1b ge4j SM	$190^{+10}_{-8}$	$120^{+6}_{-5}$	$45.6^{+3.1}_{-3.8}$	$17.1^{+2.6}_{-1.9}$	$6.8^{+1.5}_{-1.3}$	$5.4^{+1.3}_{-1.6}$	$2.4^{+0.9}_{-0.9}$	$1.2^{+0.7}_{-0.8}$
1b ge4j Data	206	135	45	14	8	6	2	0
2b ge4j SM	$73.6^{+4.2}_{-4.2}$	$45.7^{+2.8}_{-2.9}$	$20.4^{+1.8}_{-1.8}$	$7.7^{+1.2}_{-1.0}$	$1.9^{+0.3}_{-0.3}$	$0.9^{+0.2}_{-0.2}$	$0.4^{+0.1}_{-0.1}$	$0.4^{+0.1}_{-0.2}$
2b ge4j Data	79	52	31	12	1	2	0	1

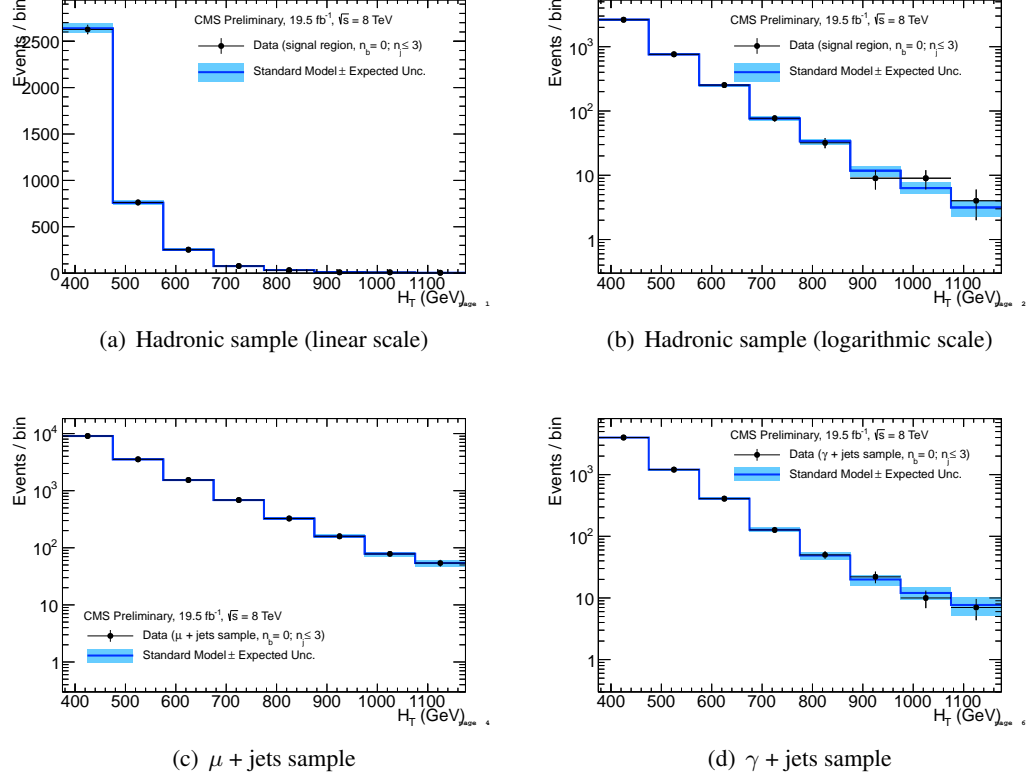


Figure 6: Comparison of the  $H_T$ -binned observed data yields and SM expectations when requiring  $2 \leq n_{\text{jet}} \leq 3$  and  $n_b = 0$  for the (a-b) hadronic, (c)  $\mu$  + jets, (d)  $\mu\mu$  + jets and (e)  $\gamma$  + jets samples, as determined by a simultaneous fit to all data samples under the SM-only hypothesis. The observed event yields in data (black dots) and the expectations and their uncertainties (dark blue solid line with light blue bands), as determined by the simultaneous fit, are shown. For illustrative purposes only, the signal expectations (pink dashed line) for the model T2cc with  $m_{\tilde{q}} = 250$  GeV and  $m_{\text{LSP}} = 240$  GeV are stacked on top of the SM expectations.



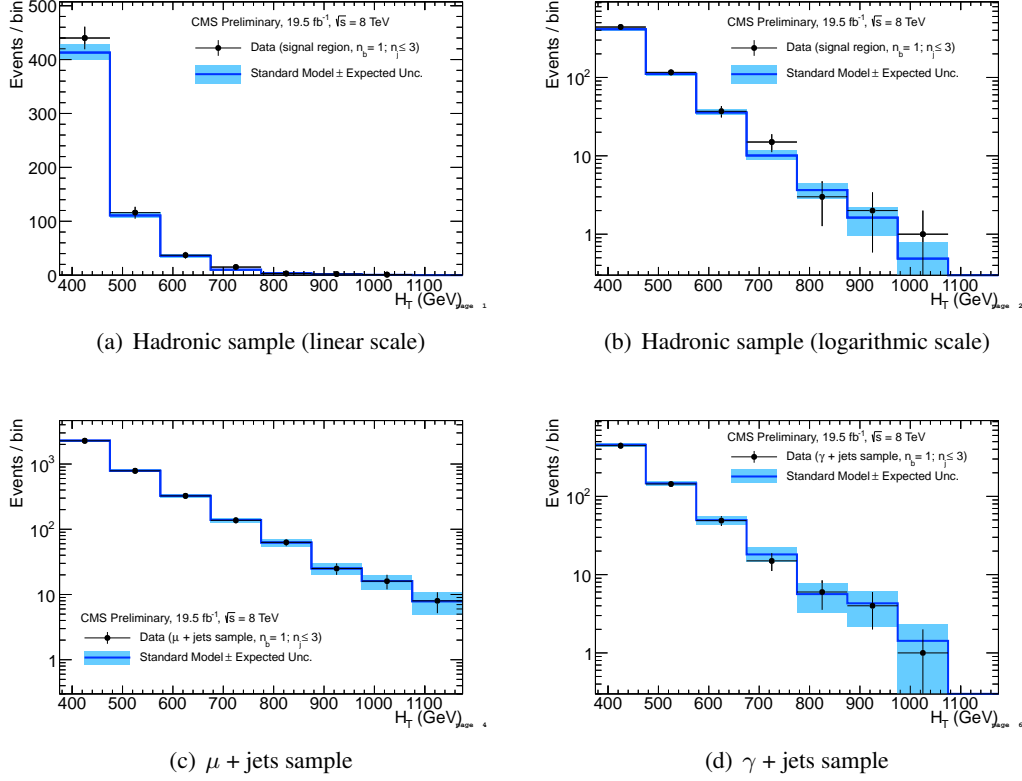


Figure 7: Comparison of the  $H_T$ -binned observed data yields and SM expectations when requiring  $2 \leq n_{\text{jet}} \leq 3$  and  $n_b = 1$  for the (a-b) hadronic, (c)  $\mu$  + jets, (d)  $\mu\mu$  + jets and (e)  $\gamma$  + jets samples, as determined by a simultaneous fit to all data samples under the SM-only hypothesis. The observed event yields in data (black dots) and the expectations and their uncertainties (dark blue solid line with light blue bands), as determined by the simultaneous fit, are shown. For illustrative purposes only, the signal expectations (pink dashed line) for the model T2cc with  $m_{\tilde{q}} = 250$  GeV and  $m_{\text{LSP}} = 170$  GeV are stacked on top of the SM expectations.

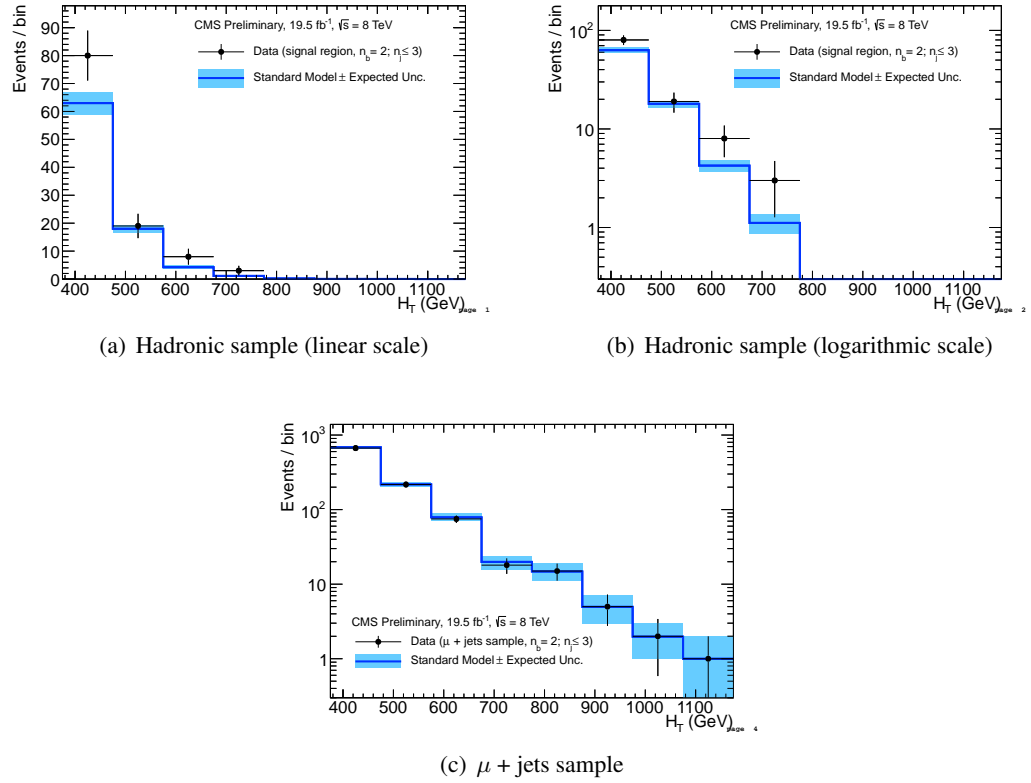


Figure 8: Comparison of the  $H_T$ -binned observed data yields and SM expectations when requiring  $2 \leq n_{jet} \leq 3$  and  $n_b = 2$  for the (a-b) hadronic and  $\mu$  + jets samples, as determined by a simultaneous fit to both the hadronic and  $\mu$  + jets data samples under the SM-only hypothesis. The observed event yields in data (black dots) and the expectations and their uncertainties (dark blue solid line with light blue bands), as determined by the simultaneous fit, are shown.

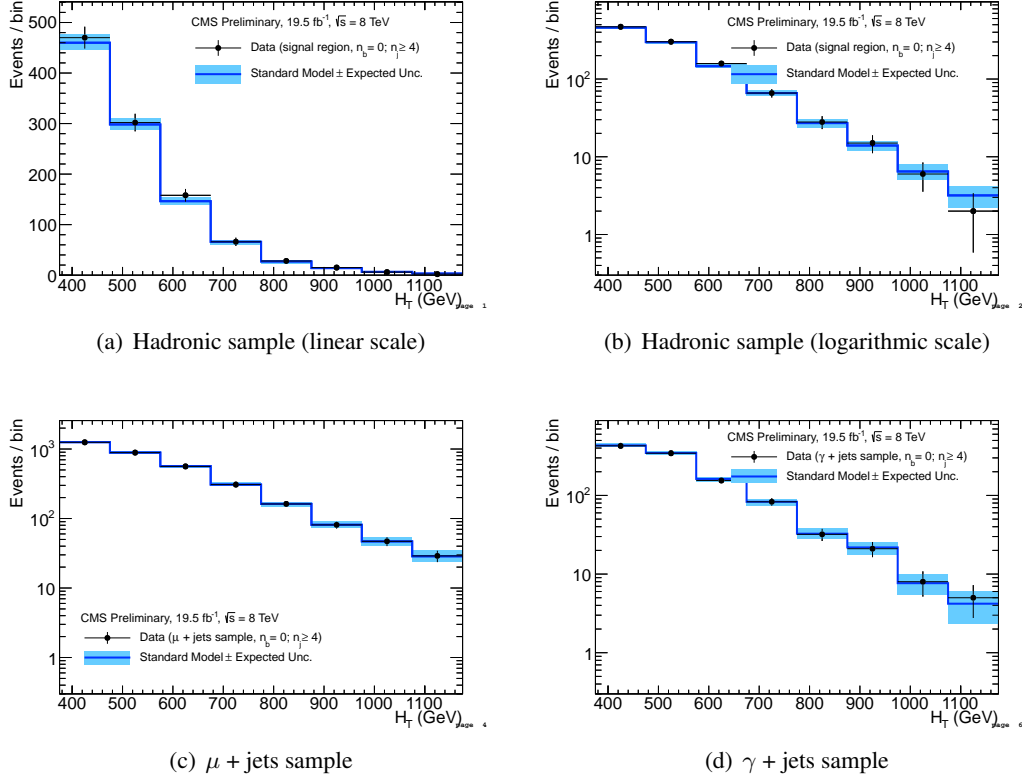


Figure 9: Comparison of the  $H_T$ -binned observed data yields and SM expectations when requiring  $n_{\text{jet}} \geq 4$  and  $n_b = 0$  for the (a-b) hadronic, (c)  $\mu + \text{jets}$ , (d)  $\mu\mu + \text{jets}$  and (e)  $\gamma + \text{jets}$  samples, as determined by a simultaneous fit to all data samples under the SM-only hypothesis. The observed event yields in data (black dots) and the expectations and their uncertainties (dark blue solid line with light blue bands), as determined by the simultaneous fit, are shown. For illustrative purposes only, the signal expectations (pink dashed line) for the model T2cc with  $m_{\tilde{q}} = 250$  GeV and  $m_{\text{LSP}} = 170$  GeV are stacked on top of the SM expectations.

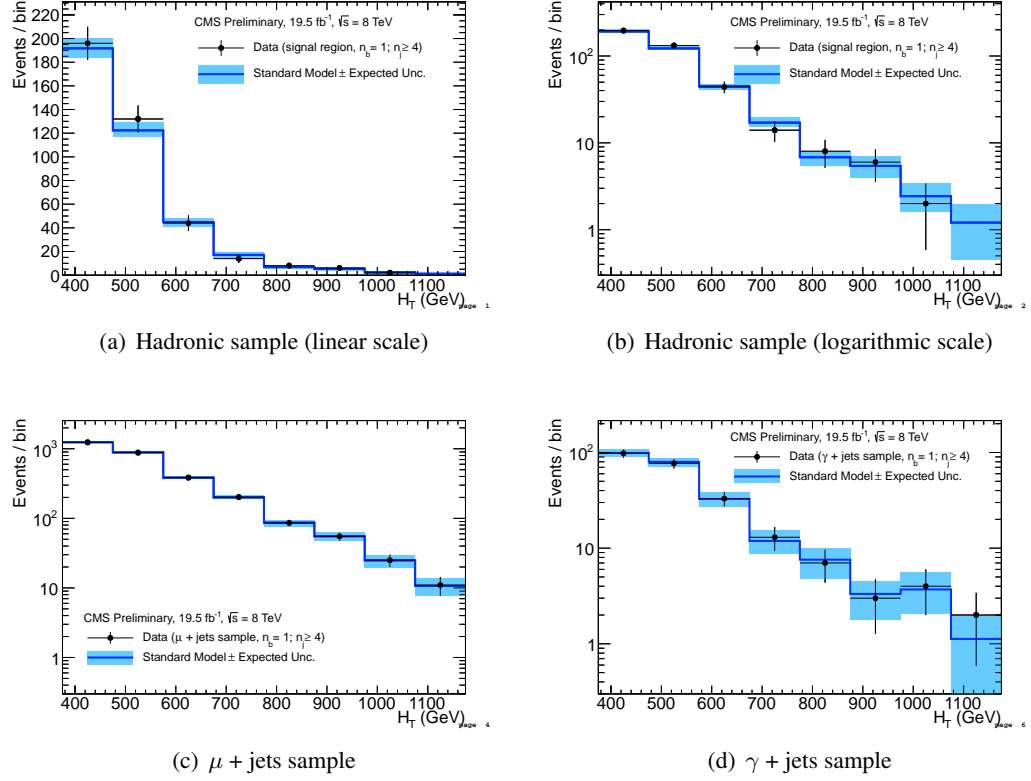


Figure 10: Comparison of the  $H_T$ -binned observed data yields and SM expectations when requiring  $n_{\text{jet}} \geq 4$  and  $n_b = 1$  for the (a-b) hadronic, (c)  $\mu$  + jets, (d)  $\mu\mu$  + jets and (e)  $\gamma$  + jets samples, as determined by a simultaneous fit to all data samples under the SM-only hypothesis. The observed event yields in data (black dots) and the expectations and their uncertainties (dark blue solid line with light blue bands), as determined by the simultaneous fit, are shown. For illustrative purposes only, the signal expectations (pink dashed line) for the model T2cc with  $m_{\tilde{q}} = 250$  GeV and  $m_{\text{LSP}} = 170$  GeV are stacked on top of the SM expectations.

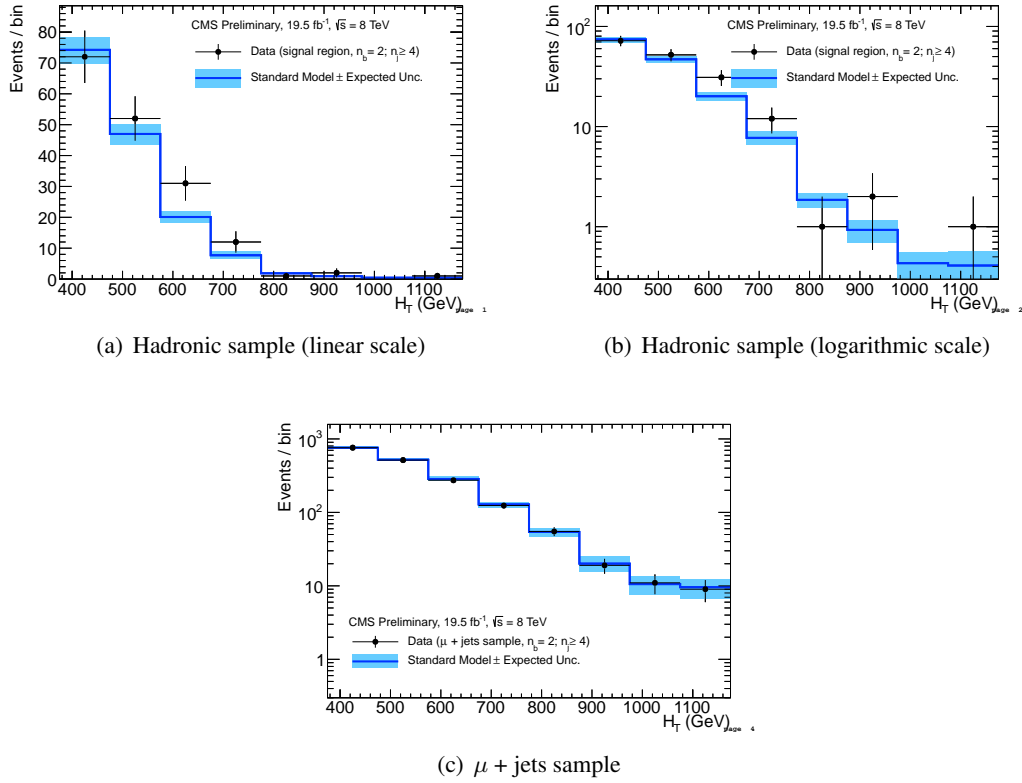


Figure 11: Comparison of the  $H_T$ -binned observed data yields and SM expectations when requiring  $n_{\text{jet}} \geq 4$  and  $n_b = 2$  for the (a-b) hadronic and  $\mu$  + jets samples, as determined by a simultaneous fit to both the hadronic and  $\mu$  + jets data samples under the SM-only hypothesis. The observed event yields in data (black dots) and the expectations and their uncertainties (dark blue solid line with light blue bands), as determined by the simultaneous fit, are shown.

## 8 Signal models and efficiencies

fill

### 8.1 Introduction

As mentioned in section ??, SUSY is a theory of many particles and parameters. Simplified models (SMS) have been derived [1, 3, 4] which reduce both particles and parameters at the cost of losing generality of the full SUSY model. Yet, SMS models are beneficial experimentally, as they provide clear signatures to search for. Two SMS models have been studied 1. T2cc: pair produced stop sparticles each decaying into a charm quark and a neutralino. 2. T2tt: pair produced stop sparticles each decaying into a top quark and a neutralino.

Event samples for the simplified models are generated by the CMS SUSY MC group [REF] at leading order with MADGRAPH [2]. The MC samples are listed in Section 4.

The SMS samples are produced in bins of stop mass ( $m_{\text{Stop}}$ ) and neutralino mass ( $m_{\text{LSP}}$ ). The analysis efficiency is studied in the usual  $n_{\text{jet}}, n_b$  binning but due to computational limitations not all categories are used to set a limit on a given model. The choice of categories for a model is made by computing the expected upper limit on the signal cross-section for each category separately using the much quicker asymptotic method [REF]. The categories are ranked by their expected upper limit. Depending on the number of mass bins and number of events per bin, two or more categories with the highest rank are chosen.

The simplified models, along with the event categories considered for each, is summarised in Table 10.

### 8.2 Efficiency times acceptance

The signal efficiency times acceptance is measured in the same binning as the analysis binning ( $n_{\text{jet}}, n_b, H_T$ ). To reduce the number of figures in this section to a manageable level, the total effi-

Table 10: A summary of the simplified models considered for interpretation. The event categories considered for each model are listed.

Model	Production/decay mode	$(n_{\text{jet}}, n_b)$ event categories considered
T2cc	$pp \rightarrow \tilde{t}\tilde{t}^* \rightarrow c\tilde{\chi}^0 \bar{c}\tilde{\chi}^0$	$(2-3,0), (\geq 4,0), (\geq 4,1)$
T2tt	$pp \rightarrow \tilde{t}\tilde{t}^* \rightarrow t\tilde{\chi}^0 \bar{t}\tilde{\chi}^0$	$(\leq 3,1), (\leq 4,2)$

ciency for only the relevant event categories and inclusive selection on  $H_T$  ( $> 200$  GeV) is shown.

Figure 12 (Appendix C.1) shows the expected signal efficiency times acceptance for the hadronic selection T2cc in the four most sensitive  $(n_{\text{jet}}, n_b)$  event categories:  $(2-3,0)$ ,  $(2-3,1)$ ,  $(\geq 4,0)$ , and  $(\geq 4,1)$ .

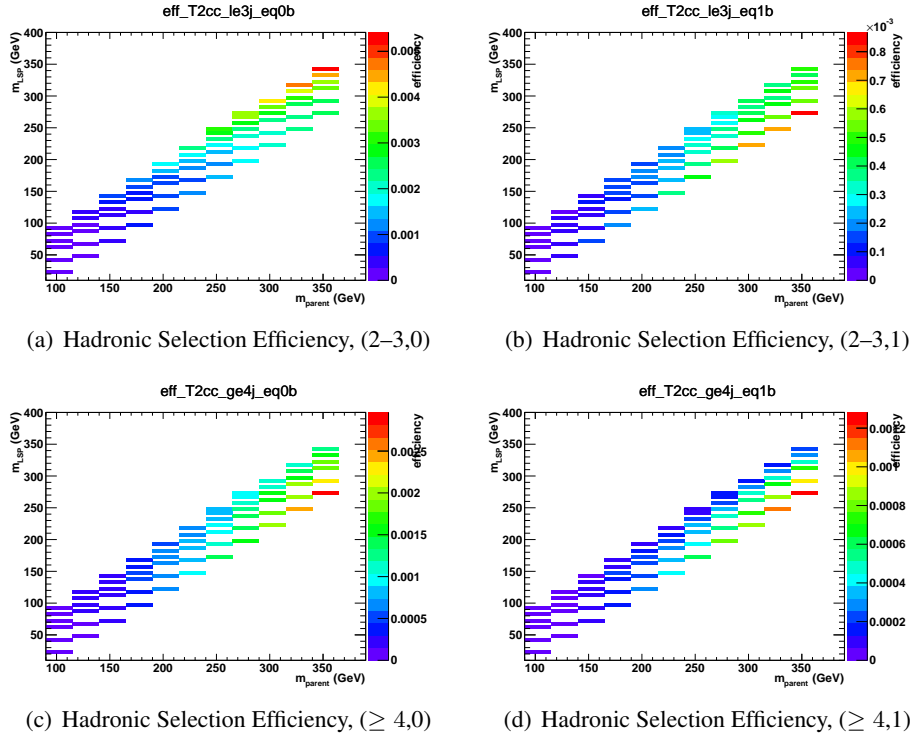


Figure 12: Hadronic selection efficiency times acceptance for T2cc for the relevant event categories defined by  $n_{\text{jet}}$  and  $n_b$ . Note the different z-axis scales.

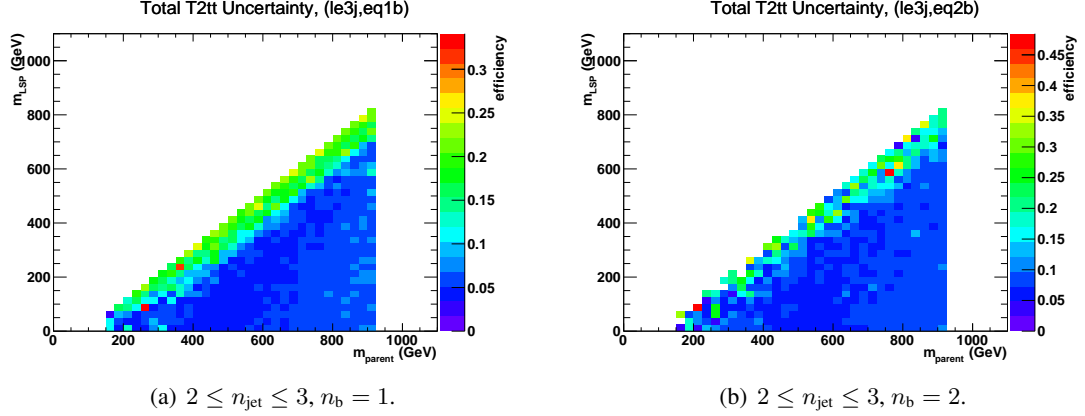


Figure 13: The total systematic uncertainty in the signal efficiency times acceptance for all relevant event categories for the T2tt interpretation.

The efficiencies are typically at the percent level or less due to reliance on hard- $p_T$  jets from initial state radiation for acceptance in the presence of a compressed mass spectrum and soft decay products. The largest efficiencies for the smallest mass splittings,  $\Delta M = \sim 10$  GeV, are obtained with the (2–3,0) category, while for larger mass splittings the (2–3,1), ( $\geq 4,0$ ), and ( $\geq 4,1$ ) categories contribute due to the reduced backgrounds in these categories. The signal efficiency in the  $\mu$  + jets control sample is negligible with respect to the signal region. By extension, the relative contamination for the  $\mu\mu$  + jets sample is also considered to be negligible. Regardless, any potential contamination is accounted for in the likelihood model.



## 9 Systematic uncertainties on signal efficiency times acceptance

### 9.1 Introduction

The systematic uncertainty in the signal acceptance times efficiency is determined per mass point per event category ( $n_{\text{jet}}, n_{\text{b}}$ ), but inclusively in  $H_{\text{T}}$  to gain statistical power. This section details the methods used to determine the magnitude of the systematic uncertainties to be applied. Four sources of uncertainty are measured: the jet energy scale, the parton distribution functions, initial state radiation and b-tag scale factors. Two other uncertainties are quoted: the uncertainty in the luminosity, measurement and the “dead ECAL” filter used in the candidate signal event selection. Each contribution is considered to be independent and all contributions are summed in quadrature to obtain a total systematic uncertainty per mass point per category.

The following sub-sections provide an overview of the various sources of uncertainty, before details on specific models are provided.

### 9.2 PDF uncertainties

The simulated signal events were produced with the CTEQ6L1 PDF set by default. As recommended by PDF4LHC [5], the uncertainty in signal efficiency due to knowledge of the PDFs is obtained by comparing the signal efficiency with that obtained with three newer alternative PDF sets: CT10, NNPDF2.1, and MSTW2008. Using the envelope formula in the reference, a single value is calculated from the three alternate PDF sets.

Figures 14 and 19 (Appendix C) show the relative difference of the signal efficiency times acceptance for the central value of the envelope calculation and the nominal PDF (CTEQ6L1) set used to produce the signal samples. The relative difference is taken as a symmetric systematic uncertainty, which varies in absolute terms within the range 0–5% across both model’s mass plane for each category of interest.

### 9.3 Jet energy scale

The relative change in the signal efficiency times acceptance is determined when varying the energy of all jets in an event up or down according to a  $p_T$ - and  $\eta$ -dependent jet energy scale uncertainty (i.e. vary the event scale up and down), as recommended by the JetMET POG. This procedure is followed per mass point per event category for an inclusive selection on  $H_T (> 375 \text{ GeV})$ .

Figures 15 and 20 (Appendix C) (Left and Middle) shows the relative change in the signal efficiency times acceptance for the relevant categories for the T2cc interpretation when varying the energy of all jets in an event up or down according to a  $p_T$ - and  $\eta$ -dependent jet energy scale uncertainty (i.e. vary the event scale up and down), as recommended by the JetMET POG. Larger variations are observed for the higher jet multiplicity category, as the jets are softer for the same requirement on  $H_T$ . Also, the variations may increase with increasing mass splitting as additional (soft) jets from the decay become hard enough to move within acceptance. Figure 15 (Right) also shows the maximum value from the up and down variations, point-by-point, which are used as the contribution to the total systematic uncertainty on the signal efficiency times acceptance. The variations are on average  $\sim 5\%$  and  $\sim 15\%$  for the low and high jet multiplicity bins, respectively, and largely independent of parent and daughter sparticle mass.

### 9.4 Initial state radiation

Signal samples produced with MADGRAPH exhibit discrepancies that have been attributed to the mismodelling of initial state radiation. These discrepancies are corrected as recommended by the SUSY PAG [10]. As per prescription, events are reweighted according to the vectorial sum of the momenta of the pair-produced sparticles. The sparticle-system  $p_T$  dependent weights are summarized in Table 11. In addition to the central weight, further variations about the central weight according to the uncertainty in the weight is applied in order to determine the systematic uncertainty associated with the correction. These systematic uncertainties are determined per mass point

per event category for an inclusive selection on  $H_T (> 375 \text{ GeV})$ . The resulting systematic uncertainties are largest near the diagonal where selected events contain significant amounts of boost due to the presence of initial state radiation.

Table 11: Sparticle system  $p_T$  dependent corrections and systematic weight variations.

Sparticle system $p_T$ (GeV)	Central Weight	Systematic Variation
$0 < p_T < 120$	1.00	$\pm 0.0$
$120 < p_T < 150$	0.95	$\pm 0.05$
$150 < p_T < 250$	0.90	$\pm 0.10$
$p_T > 250$	0.80	$\pm 0.20$

## 9.5 b-tag scale factor corrections

The uncertainty on the btag scale factors described in section [REF] is calculated by varying the scale factors up and down by their uncertainty as described in Ref. [? ]. where the relevant dependences are implied. Once all events have been reweighted this way, the yields in each  $b$ -tag bin represent the corrected MC yields.

## 9.6 Systematic uncertainties for T2cc

Figure 16 (Left and Middle) shows the relative change in the signal efficiency times acceptance for the relevant categories for the T2cc interpretation when varying up and down the sparticle system  $p_T$ -dependent corrections by their uncertainties. The largest variations, up to  $\sim 25\%$  are observed for the smallest mass splittings, when the reliance on ISR jets for acceptance is largest. Figure 16 (Right) also shows the maximum value from the up and down variations, point-by-point, which are used as the contribution to the total systematic uncertainty on the signal efficiency times acceptance. This is the most dominant contribution to the total.

Figure 17 (Left and Middle) shows the relative change in the signal efficiency times acceptance for the relevant categories for the T2cc interpretation when varying up and down the scale-factor

corrections by their uncertainties. The variations are anti-correlated for the two  $n_b$  categories used by this interpretation and are generally small, at the level of 1–5%, with respect to other contributions. Figure 17 (Right) shows the maximum value from the up and down variations, point-by-point, which are used as the contribution to the total systematic uncertainty on the signal efficiency times acceptance.

Table 14 presents a *representative* range of values for the contribution to the total systematic uncertainty in the signal efficiency times acceptance for each relevant event category. An uncertainty of 2.3% in the integrated luminosity is also considered. An uncertainty of 4% from increasing the number of associated partons (from 2 to 3) in the scan is also considered. The contribution from PDF uncertainties are determined for an inclusive selection on  $n_{\text{jet}}$  and  $n_b$  only. Figure 18 shows the total systematic uncertainty in the T2cc mass plane for the relevant categories.

Table 12: Representative ranges for each contribution to the total systematic uncertainty in the signal efficiency times acceptance for each relevant event category for the T2cc interpretation. See text for further details on other (fixed) contributions to the total systematic uncertainty.

Category	(2–3,0)		$(\geq 4,0)$		$(\geq 4,1)$		$(\geq 2, \geq 0)$	
Range	Min.	Max.	Min.	Max.	Min.	Max.	Min.	Max.
PDF							0.04	0.14
JES	0.00	0.08	0.06	0.22	0.01	0.30		
ISR	0.09	0.21	0.16	0.24	0.15	0.24		
b-tag SF	0.01	0.02	0.01	0.02	0.03	0.04		
Dead ECAL	0.02	0.02	0.02	0.02	0.02	0.02		
Total syst	0.12	0.21	0.22	0.32	0.23	0.39		

## 9.7 Systematic uncertainties for T2tt

Figure 19 (Appendix C.2) shows the ratio of the signal efficiency times acceptance for the central value and  $\pm 1\sigma$  variations of the envelope calculation relative to the nominal PDF (CTEQ6L1) set

used to produce the T2cc sample. The relative difference (based on the central value of the envelope calculation) is currently taken as a (symmetric) systematic uncertainty, which varies in absolute terms within the range 0–10% across the T2cc mass plane, with the largest positive changes at the smallest top squark mass of 100 GeV. The systematic uncertainty is determined independently of  $n_{\text{jet}}$  and  $n_b$  and is used for all  $H_T$  bins (a conservative approach). Any systematic uncertainties resulting from changes in the signal shape are considered to be negligible, as discussed in Section 9.2

Figures ?? and ?? show the relative change in the signal efficiency times acceptance for the relevant categories for the T2cc interpretation when varying the energy of all jets in an event up or down according to a  $p_T$ - and  $\eta$ -dependent jet energy scale uncertainty (i.e. vary the event scale up and down), as recommended by the JetMET POG. Larger variations are observed for the higher jet multiplicity category, as the jets are softer for the same requirement on  $H_T$ . Also, the variations may increase with increasing mass splitting as additional (soft) jets from the decay become hard enough to move within acceptance. Figure 15 shows the maximum value from the up and down variations, point-by-point, which are used as the contribution to the total systematic uncertainty on the signal efficiency times acceptance.

Figures ?? and ?? show the relative change in the signal efficiency times acceptance for the relevant categories for the T2cc interpretation when varying (up and down) the sparticle system  $p_T$ -dependent corrections by their uncertainties. The largest variations, up to  $\sim 20\%$  are observed for the smallest mass splittings, when the reliance on ISR jets for acceptance is largest. Figure 16 shows the maximum value from the up and down variations, point-by-point, which are used as the contribution to the total systematic uncertainty on the signal efficiency times acceptance. This is the most dominant contribution to the total.

Figures ?? and ?? show the relative change in the signal efficiency times acceptance for the relevant categories for the T2cc interpretation when varying (up and down) the scale-factor cor-

rections by their uncertainties. The variations are anti-correlated for the two  $n_b$  categories used by this interpretation and are generally small, at the level of 2–4%, with respect to other contributions. Figure 17 shows the maximum value from the up and down variations, point-by-point, which are used as the contribution to the total systematic uncertainty on the signal efficiency times acceptance.

The contribution from uncertainties in the efficiency of the  $H_T/E_T < 1.25$  requirement is expected to be sub-dominant with respect to other contributions, and is estimated to be at the level of 0–2% as discussed in Section ???. It is however useful to inspect the expected efficiency of this requirement for the T2cc model to see if the behaviour is comparable to that observed in data and the FullSim simulation. Figure ?? shows the efficiency of the  $H_T/E_T < 1.25$  requirement for the relevant categories for the T2cc interpretation. The efficiency is observed to be  $\sim 90$ –97% for the region  $m_{\text{stop}} > 200$  GeV and the smallest mass splittings, dropping to  $\sim 80$ % for smaller mass values in the region  $100 < m_{\text{stop}} < 200$  GeV. Lower efficiencies are observed for the larger mass splittings (and smaller  $m_{\text{stop}}$ ), typically in the range 70–90%. This is likely due to soft jets from the SUSY decay within acceptance degrading the resolution of the  $H_T$  variable, hence the requirement on  $H_T/E_T$  becomes effectively tighter.

The contribution from uncertainties in the efficiency of the dead ECAL filter is expected to be sub-dominant with respect to other contributions, and is estimated to be at the level of 0–2% as discussed in Section ???. Figure ?? shows the efficiency of the dead ECAL filter for the relevant categories for the T2cc interpretation. The efficiency is observed to be insensitive to the mass splitting and increasing from 92% to 97% (70% to 93%) with  $m_{\text{stop}}$  for events satisfying  $2 \leq n_{\text{jet}} \leq 3$  ( $n_{\text{jet}} \geq 4$ ).

Finally, the T2cc sample are produced using MADGRAPH as the matrix level generator. The scan is produced with up to two associated partons at the generator level. Given the relatively high sensitivity to initial state radiation in the signal phase space, a validation scan was produced

with up to three associated partons. The scan comprises two mass points with  $m_{\text{stop}} = 200 \text{ GeV}$  and an LSP mass of 120 GeV and 190 GeV in order to cover the full range in mass splittings (i.e.  $\Delta m = 10 \text{ and } 80 \text{ GeV}$ ). The ratio of acceptances between the 3-parton scan relative to the default 2-parton scan for these two mass points are shown in Table 13. These values are interpreted as contributions to the systematic uncertainty on the efficiency times acceptance, and the largest relative change, 4%, is applied across the full mass plane for all event categories.

Table 13: Relative change in efficiency times acceptance for the 2-parton and 3-parton scans. The points have a stop mass of 200 GeV and cover two different  $\Delta m$  points.

Category	$\Delta m \text{ (GeV)}$	
	10	80
(2–3,0)	0.00	0.04
(2–3,1)	0.02	0.04
( $\geq 4$ ,0)	0.04	0.04
( $\geq 4$ ,1)	0.00	0.00

Table 14 presents a *representative* range of values for the contribution to the total systematic uncertainty in the signal efficiency times acceptance for each relevant event category. An uncertainty of 2.3% in the integrated luminosity is also considered. An uncertainty of 4% from increasing the number of associated partons (from 2 to 3) in the scan is also considered. The contribution from PDF uncertainties are determined for an inclusive selection on  $n_{\text{jet}}$  and  $n_b$  only. Figure 18 shows the total systematic uncertainty in the T2cc mass plane for the relevant categories.

Table 14: Representative ranges for each contribution to the total systematic uncertainty in the signal efficiency times acceptance for each relevant event category for the T2cc interpretation. See text for further details on other (fixed) contributions to the total systematic uncertainty.

Category	(2–3,0)		$(\geq 4,0)$		$(\geq 4,1)$		$(\geq 2, \geq 0)$	
Range	Min.	Max.	Min.	Max.	Min.	Max.	Min.	Max.
PDF							0.04	0.14
JES	0.00	0.08	0.06	0.22	0.01	0.30		
ISR	0.09	0.21	0.16	0.24	0.15	0.24		
b-tag SF	0.01	0.02	0.01	0.02	0.03	0.04		
$H_T/E_T$	0.02	0.02	0.02	0.02	0.02	0.02		
Dead ECAL	0.02	0.02	0.02	0.02	0.02	0.02		
Total syst	0.12	0.21	0.22	0.32	0.23	0.39		



## A Maximum likelihood parameter values

Table 15: SM-only maximum-likelihood parameter values (0b le3j).

name	value	error
$\text{EWK}^0$	2.64e+03	4.7e+01
$\text{EWK}^1$	7.59e+02	2.2e+01
$\text{EWK}^2$	2.52e+02	1.1e+01
$\text{EWK}^3$	7.64e+01	6.0e+00
$\text{EWK}^4$	3.37e+01	3.5e+00
$\text{EWK}^5$	1.18e+01	2.0e+00
$\text{EWK}^6$	6.32e+00	1.4e+00
$\text{EWK}^7$	3.15e+00	8.9e-01
$f_{\text{Zinv}}^0$	0.64	0.02
$f_{\text{Zinv}}^1$	0.67	0.02
$f_{\text{Zinv}}^2$	0.70	0.02
$f_{\text{Zinv}}^3$	0.70	0.04
$f_{\text{Zinv}}^4$	0.69	0.04
$f_{\text{Zinv}}^5$	0.76	0.05
$f_{\text{Zinv}}^6$	0.76	0.06
$f_{\text{Zinv}}^7$	0.82	0.06
$\rho_{\mu W}^0$	1.01	0.05
$\rho_{\mu W}^1$	1.00	0.06
$\rho_{\mu W}^2$	1.00	0.07
$\rho_{\mu W}^3$	1.00	0.11
$\rho_{\mu W}^4$	1.01	0.11
$\rho_{\mu W}^5$	1.02	0.16
$\rho_{\mu W}^6$	0.98	0.15
$\rho_{\mu W}^7$	1.00	0.16
$\rho_{\gamma Z}^0$	1.02	0.04
$\rho_{\gamma Z}^1$	0.99	0.04
$\rho_{\gamma Z}^2$	1.00	0.06
$\rho_{\gamma Z}^3$	0.99	0.10
$\rho_{\gamma Z}^4$	1.02	0.11
$\rho_{\gamma Z}^5$	1.05	0.16
$\rho_{\gamma Z}^6$	0.95	0.14
$\rho_{\gamma Z}^7$	0.98	0.15

Table 16: SM-only maximum-likelihood parameter values (1b 1e3j).

name	value	error
$\text{EWK}^0$	4.13e+02	1.4e+01
$\text{EWK}^1$	1.11e+02	5.9e+00
$\text{EWK}^2$	3.58e+01	3.0e+00
$\text{EWK}^3$	1.01e+01	1.6e+00
$\text{EWK}^4$	3.66e+00	8.2e-01
$\text{EWK}^5$	1.63e+00	6.0e-01
$\text{EWK}^6$	4.87e-01	3.1e-01
$\text{EWK}^7$	1.21e-01	4.7e-02
$f_{\text{Zinv}}^0$	0.47	0.02
$f_{\text{Zinv}}^1$	0.55	0.03
$f_{\text{Zinv}}^2$	0.57	0.04
$f_{\text{Zinv}}^3$	0.64	0.07
$f_{\text{Zinv}}^4$	0.55	0.11
$f_{\text{Zinv}}^5$	0.81	0.08
$f_{\text{Zinv}}^6$	0.82	0.12
$f_{\text{Zinv}}^7$	0.00	0.83
$\rho_{\mu W}^0$	0.95	0.05
$\rho_{\mu W}^1$	0.99	0.06
$\rho_{\mu W}^2$	1.00	0.07
$\rho_{\mu W}^3$	0.98	0.11
$\rho_{\mu W}^4$	1.00	0.11
$\rho_{\mu W}^5$	1.00	0.16
$\rho_{\mu W}^6$	1.00	0.16
$\rho_{\mu W}^7$	1.00	0.16
$\rho_{\gamma Z}^0$	0.96	0.05
$\rho_{\gamma Z}^1$	0.99	0.06
$\rho_{\gamma Z}^2$	1.00	0.07
$\rho_{\gamma Z}^3$	0.96	0.11
$\rho_{\gamma Z}^4$	1.00	0.11
$\rho_{\gamma Z}^5$	0.99	0.15
$\rho_{\gamma Z}^6$	0.99	0.15
$\rho_{\gamma Z}^7$	1.00	0.16

Table 17: SM-only maximum-likelihood parameter values (2b le3j).

name	value	error
$\text{EWK}^0$	6.30e+01	3.8e+00
$\text{EWK}^1$	1.80e+01	1.5e+00
$\text{EWK}^2$	4.25e+00	5.4e-01
$\text{EWK}^3$	1.11e+00	2.7e-01
$\text{EWK}^4$	2.10e-01	5.9e-02
$\text{EWK}^5$	3.83e-02	1.8e-02
$\text{EWK}^6$	2.33e-02	1.7e-02
$\text{EWK}^7$	1.30e-03	1.3e-03
$\rho_{\mu W}^0$	0.94	0.05
$\rho_{\mu W}^1$	1.00	0.06
$\rho_{\mu W}^2$	0.98	0.07
$\rho_{\mu W}^3$	0.98	0.11
$\rho_{\mu W}^4$	1.00	0.11
$\rho_{\mu W}^5$	1.00	0.16
$\rho_{\mu W}^6$	1.00	0.16
$\rho_{\mu W}^7$	1.00	0.16

Table 18: SM-only maximum-likelihood parameter values (0b ge4j).

name	value	error
$\text{EWK}^0$	4.60e+02	1.6e+01
$\text{EWK}^1$	2.98e+02	1.2e+01
$\text{EWK}^2$	1.46e+02	8.2e+00
$\text{EWK}^3$	6.59e+01	5.7e+00
$\text{EWK}^4$	2.71e+01	3.3e+00
$\text{EWK}^5$	1.39e+01	2.2e+00
$\text{EWK}^6$	6.47e+00	1.5e+00
$\text{EWK}^7$	3.19e+00	9.5e-01
$f_{\text{Zinv}}^0$	0.52	0.02
$f_{\text{Zinv}}^1$	0.60	0.02
$f_{\text{Zinv}}^2$	0.61	0.03
$f_{\text{Zinv}}^3$	0.63	0.05
$f_{\text{Zinv}}^4$	0.71	0.05
$f_{\text{Zinv}}^5$	0.73	0.06
$f_{\text{Zinv}}^6$	0.74	0.07
$f_{\text{Zinv}}^7$	0.67	0.11
$\rho_{\mu W}^0$	0.98	0.05
$\rho_{\mu W}^1$	1.00	0.06
$\rho_{\mu W}^2$	0.97	0.07
$\rho_{\mu W}^3$	1.00	0.13
$\rho_{\mu W}^4$	1.00	0.13
$\rho_{\mu W}^5$	1.00	0.13
$\rho_{\mu W}^6$	1.00	0.13
$\rho_{\mu W}^7$	1.01	0.19
$\rho_{\gamma Z}^0$	0.98	0.05
$\rho_{\gamma Z}^1$	0.99	0.05
$\rho_{\gamma Z}^2$	0.96	0.07
$\rho_{\gamma Z}^3$	1.00	0.11
$\rho_{\gamma Z}^4$	0.99	0.12
$\rho_{\gamma Z}^5$	0.99	0.12
$\rho_{\gamma Z}^6$	1.01	0.13
$\rho_{\gamma Z}^7$	1.03	0.19

Table 19: SM-only maximum-likelihood parameter values (1b ge4j).

name	value	error
$\text{EWK}^0$	1.92e+02	8.5e+00
$\text{EWK}^1$	1.22e+02	6.1e+00
$\text{EWK}^2$	4.48e+01	3.5e+00
$\text{EWK}^3$	1.71e+01	2.1e+00
$\text{EWK}^4$	6.82e+00	1.3e+00
$\text{EWK}^5$	5.43e+00	1.5e+00
$\text{EWK}^6$	2.43e+00	7.9e-01
$\text{EWK}^7$	1.21e+00	6.3e-01
$f_{\text{Zinv}}^0$	0.23	0.02
$f_{\text{Zinv}}^1$	0.29	0.03
$f_{\text{Zinv}}^2$	0.38	0.05
$f_{\text{Zinv}}^3$	0.36	0.08
$f_{\text{Zinv}}^4$	0.49	0.10
$f_{\text{Zinv}}^5$	0.58	0.12
$f_{\text{Zinv}}^6$	0.70	0.11
$f_{\text{Zinv}}^7$	0.72	0.16
$\rho_{\mu W}^0$	0.99	0.05
$\rho_{\mu W}^1$	0.98	0.05
$\rho_{\mu W}^2$	1.00	0.07
$\rho_{\mu W}^3$	1.03	0.13
$\rho_{\mu W}^4$	0.99	0.13
$\rho_{\mu W}^5$	1.00	0.13
$\rho_{\mu W}^6$	1.00	0.13
$\rho_{\mu W}^7$	1.01	0.19
$\rho_{\gamma Z}^0$	1.00	0.06
$\rho_{\gamma Z}^1$	0.99	0.06
$\rho_{\gamma Z}^2$	1.00	0.08
$\rho_{\gamma Z}^3$	1.02	0.13
$\rho_{\gamma Z}^4$	0.99	0.13
$\rho_{\gamma Z}^5$	0.99	0.13
$\rho_{\gamma Z}^6$	1.01	0.13
$\rho_{\gamma Z}^7$	1.03	0.19

Table 20: SM-only maximum-likelihood parameter values (2b ge4j).

name	value	error
$\text{EWK}^0$	7.42e+01	4.4e+00
$\text{EWK}^1$	4.70e+01	3.1e+00
$\text{EWK}^2$	2.01e+01	1.8e+00
$\text{EWK}^3$	7.71e+00	1.1e+00
$\text{EWK}^4$	1.85e+00	3.4e-01
$\text{EWK}^5$	9.29e-01	2.3e-01
$\text{EWK}^6$	4.32e-01	1.4e-01
$\text{EWK}^7$	4.09e-01	1.5e-01
$\rho_{\mu W}^0$	1.01	0.05
$\rho_{\mu W}^1$	0.98	0.05
$\rho_{\mu W}^2$	0.94	0.07
$\rho_{\mu W}^3$	0.93	0.11
$\rho_{\mu W}^4$	1.01	0.13
$\rho_{\mu W}^5$	0.98	0.13
$\rho_{\mu W}^6$	1.01	0.13
$\rho_{\mu W}^7$	0.98	0.18

## B SM-only yield tables

The following tables compare the observations in the hadronic and control samples with the maximum-likelihood expectations obtained by the SM-only fit.

Table 21: 0b 1e3j

$H_T$ Bin (GeV)	375–475	475–575	575–675	675–775	775–875	875–975	975–1075	1075– $\infty$
SM hadronic	$2744^{+48}_{-43}$	$771^{+21}_{-23}$	$254^{+13}_{-13}$	$76.5^{+6.1}_{-4.8}$	$33.7^{+3.7}_{-3.8}$	$11.8^{+1.9}_{-2.1}$	$6.3^{+1.4}_{-1.3}$	$3.2^{+1.0}_{-0.9}$
Data hadronic	2728	766	257	77	32	9	9	4
SM $\mu$ +jets	$9072^{+97}_{-113}$	$3543^{+56}_{-62}$	$1539^{+39}_{-41}$	$686^{+25}_{-26}$	$325^{+17}_{-17}$	$158^{+13}_{-12}$	$78.6^{+7.8}_{-8.3}$	$54.1^{+7.0}_{-6.8}$
Data $\mu$ +jets	9078	3545	1538	686	326	159	78	54
SM $\gamma$ +jets	$3990^{+54}_{-61}$	$1203^{+34}_{-37}$	$410^{+17}_{-19}$	$127^{+10}_{-10}$	$48.8^{+6.0}_{-6.9}$	$19.9^{+3.3}_{-4.2}$	$12.1^{+3.0}_{-2.9}$	$7.7^{+2.9}_{-2.7}$
Data $\gamma$ +jets	4000	1206	408	127	50	22	10	7

Table 22: 0b ge4j

$H_T$ Bin (GeV)	375–475	475–575	575–675	675–775	775–875	875–975	975–1075	1075– $\infty$
SM hadronic	$456^{+15}_{-14}$	$291^{+12}_{-12}$	$148^{+8}_{-7}$	$66.0^{+5.6}_{-5.2}$	$27.1^{+2.9}_{-3.4}$	$14.0^{+1.9}_{-2.1}$	$6.5^{+1.5}_{-1.2}$	$3.2^{+1.0}_{-0.9}$
Data hadronic	480	299	158	66	28	15	6	2
SM $\mu$ +jets	$1260^{+36}_{-36}$	$891^{+29}_{-30}$	$566^{+23}_{-23}$	$308^{+20}_{-14}$	$162^{+11}_{-12}$	$81.3^{+8.6}_{-8.1}$	$46.9^{+7.3}_{-6.1}$	$28.6^{+6.4}_{-4.4}$
Data $\mu$ +jets	1249	888	562	308	162	81	47	29
SM $\gamma$ +jets	$439^{+20}_{-18}$	$349^{+16}_{-18}$	$161^{+10}_{-13}$	$83.0^{+7.9}_{-8.5}$	$32.6^{+5.7}_{-5.6}$	$21.8^{+3.6}_{-4.2}$	$7.7^{+2.4}_{-2.0}$	$4.2^{+1.7}_{-1.7}$
Data $\gamma$ +jets	427	344	155	83	32	21	8	5



Table 23: 1b le3j

$H_T$ Bin (GeV)	375–475	475–575	575–675	675–775	775–875	875–975	975–1075	1075– $\infty$
SM hadronic	$426^{+15}_{-17}$	$114^{+6}_{-6}$	$35.5^{+3.3}_{-2.8}$	$10.1^{+1.4}_{-1.5}$	$3.7^{+0.9}_{-0.8}$	$1.6^{+0.7}_{-0.6}$	$0.5^{+0.3}_{-0.4}$	$0.1^{+0.1}_{-0.0}$
Data hadronic	444	118	36	15	3	2	1	0
SM $\mu$ +jets	$2282^{+50}_{-45}$	$789^{+26}_{-27}$	$325^{+20}_{-17}$	$139^{+11}_{-14}$	$62.7^{+9.2}_{-6.5}$	$25.1^{+4.8}_{-5.1}$	$16.1^{+3.9}_{-4.1}$	$7.9^{+2.9}_{-2.9}$
Data $\mu$ +jets	2272	787	325	137	63	25	16	8
SM $\gamma$ +jets	$452^{+20}_{-22}$	$146^{+9}_{-10}$	$49.3^{+6.6}_{-5.9}$	$18.1^{+3.8}_{-4.4}$	$5.6^{+2.4}_{-2.4}$	$4.3^{+1.9}_{-1.8}$	$1.4^{+1.0}_{-1.4}$	$0.0^{+0.0}_{-0.0}$
Data $\gamma$ +jets	444	144	49	15	6	4	1	0

Table 24: 1b ge4j

$H_T$ Bin (GeV)	375–475	475–575	575–675	675–775	775–875	875–975	975–1075	1075– $\infty$
SM hadronic	$190^{+10}_{-8}$	$120^{+6}_{-5}$	$45.6^{+3.1}_{-3.8}$	$17.1^{+2.6}_{-1.9}$	$6.8^{+1.5}_{-1.3}$	$5.4^{+1.3}_{-1.6}$	$2.4^{+0.9}_{-0.9}$	$1.2^{+0.7}_{-0.8}$
Data hadronic	206	135	45	14	8	6	2	0
SM $\mu$ +jets	$1250^{+37}_{-28}$	$891^{+27}_{-31}$	$385^{+21}_{-20}$	$200^{+12}_{-12}$	$86.6^{+9.0}_{-10.1}$	$55.3^{+7.7}_{-7.3}$	$24.9^{+4.4}_{-5.3}$	$10.7^{+3.1}_{-3.4}$
Data $\mu$ +jets	1238	881	385	202	86	55	25	11
SM $\gamma$ +jets	$102^{+10}_{-9}$	$81.3^{+8.2}_{-7.9}$	$32.7^{+5.5}_{-5.6}$	$11.9^{+3.7}_{-3.0}$	$7.6^{+2.6}_{-2.6}$	$3.3^{+1.2}_{-1.6}$	$3.7^{+1.9}_{-1.9}$	$1.1^{+0.8}_{-1.1}$
Data $\gamma$ +jets	98	77	33	13	7	3	4	2

Table 25: 2b le3j

$H_T$ Bin (GeV)	375–475	475–575	575–675	675–775	775–875	875–975	975–1075	1075– $\infty$
SM hadronic	$65.0^{+4.3}_{-4.3}$	$18.4^{+1.7}_{-1.6}$	$4.2^{+0.6}_{-0.5}$	$1.1^{+0.3}_{-0.2}$	$0.2^{+0.1}_{-0.1}$	$0.0^{+0.0}_{-0.0}$	$0.0^{+0.0}_{-0.0}$	$0.0^{+0.0}_{-0.0}$
Data hadronic	78	18	8	3	0	0	0	0
SM $\mu$ +jets	$681^{+26}_{-31}$	$217^{+14}_{-14}$	$78.8^{+9.4}_{-9.3}$	$19.9^{+4.1}_{-3.8}$	$14.8^{+4.0}_{-3.9}$	$5.0^{+2.0}_{-2.1}$	$2.0^{+1.0}_{-1.0}$	$1.0^{+1.0}_{-1.0}$
Data $\mu$ +jets	668	217	75	18	15	5	2	1
Data $\gamma$ +jets	36	8	4	0	0	1	0	0

Table 26: 2b ge4j

$H_T$ Bin (GeV)	375–475	475–575	575–675	675–775	775–875	875–975	975–1075	1075– $\infty$
SM hadronic	$73.6^{+4.2}_{-4.2}$	$45.7^{+2.8}_{-2.9}$	$20.4^{+1.8}_{-1.8}$	$7.7^{+1.2}_{-1.0}$	$1.9^{+0.3}_{-0.3}$	$0.9^{+0.2}_{-0.2}$	$0.4^{+0.1}_{-0.1}$	$0.4^{+0.1}_{-0.2}$
Data hadronic	79	52	31	12	1	2	0	1
SM $\mu$ +jets	$765^{+26}_{-27}$	$521^{+23}_{-22}$	$285^{+15}_{-17}$	$128^{+12}_{-10}$	$54.1^{+7.5}_{-8.0}$	$20.1^{+4.6}_{-4.1}$	$10.6^{+2.9}_{-2.9}$	$9.6^{+2.9}_{-2.9}$
Data $\mu$ +jets	760	515	274	124	55	19	11	9
Data $\gamma$ +jets	19	17	10	4	0	2	1	0

## C Efficiencies and systematic uncertainties for simplified models

### C.1 T2cc

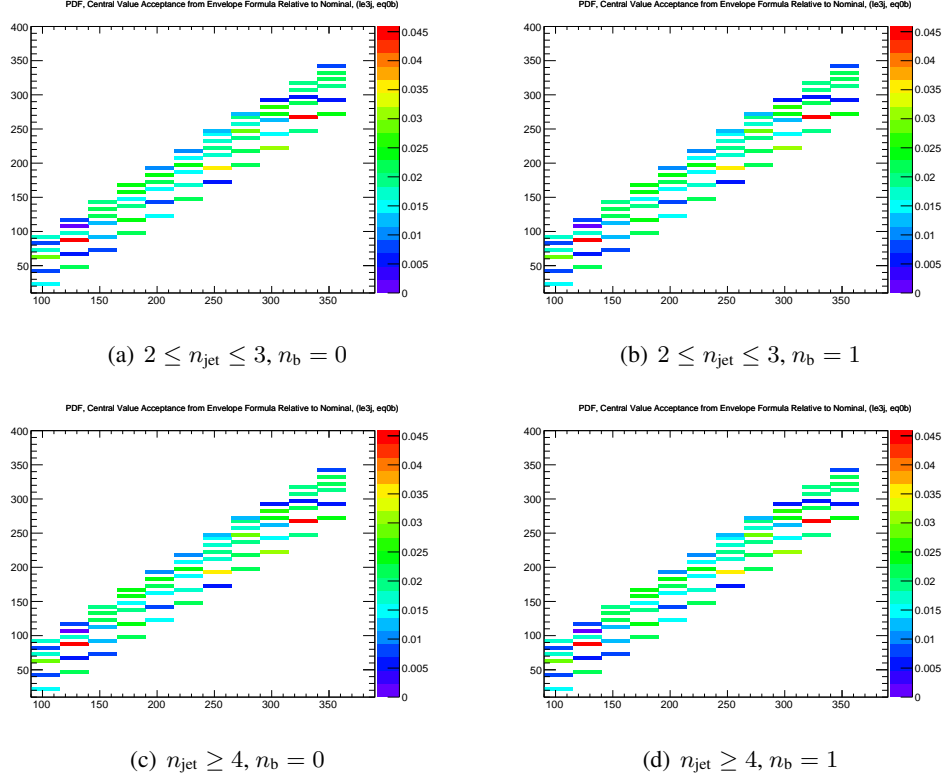


Figure 14: Ratio of efficiency times acceptance for the (middle) central value, (top)  $+1\sigma$  value, (bottom)  $-1\sigma$  value of the envelope calculation relative to the nominal PDF set used to produce the T2cc sample.

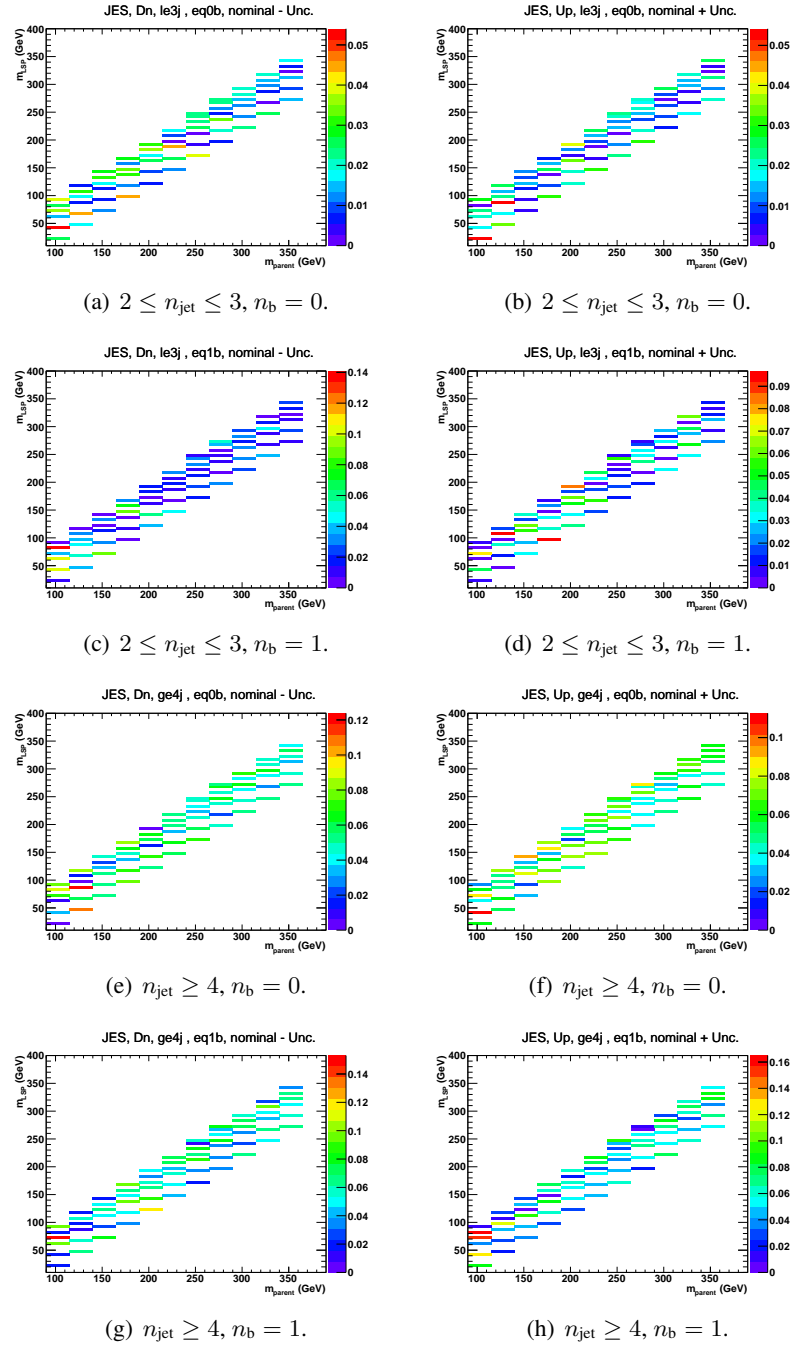


Figure 15: The fractional change in signal efficiency due to systematically (Left) increasing and (Middle) decreasing all jet energies, and (Right) the resulting (symmetric) systematic uncertainties due to JES uncertainties for T2cc.

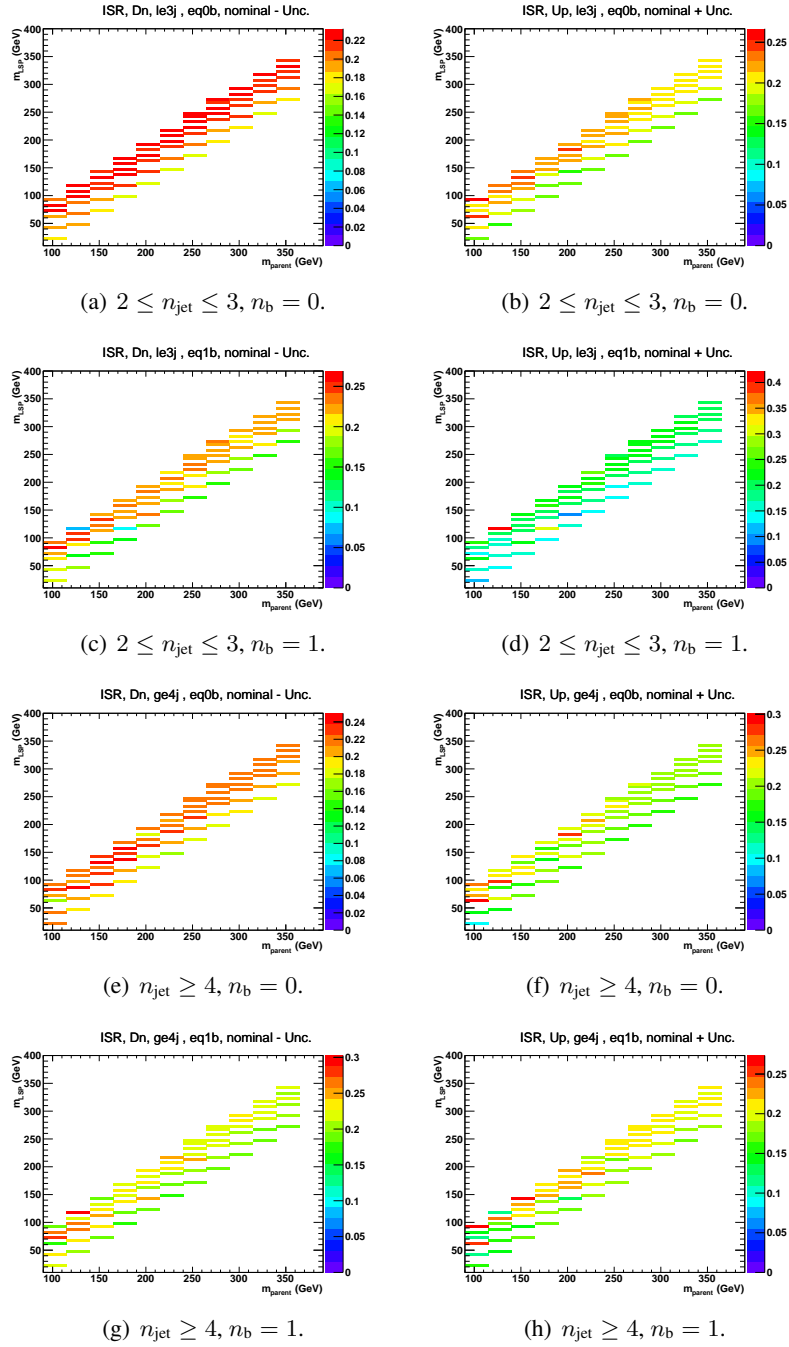


Figure 16: The fractional change in signal efficiency due to systematically (Left) increasing and (Middle) decreasing event weights according to ISR uncertainties, and (Right) the resulting (symmetric) systematic uncertainties due to ISR uncertainties for T2cc.

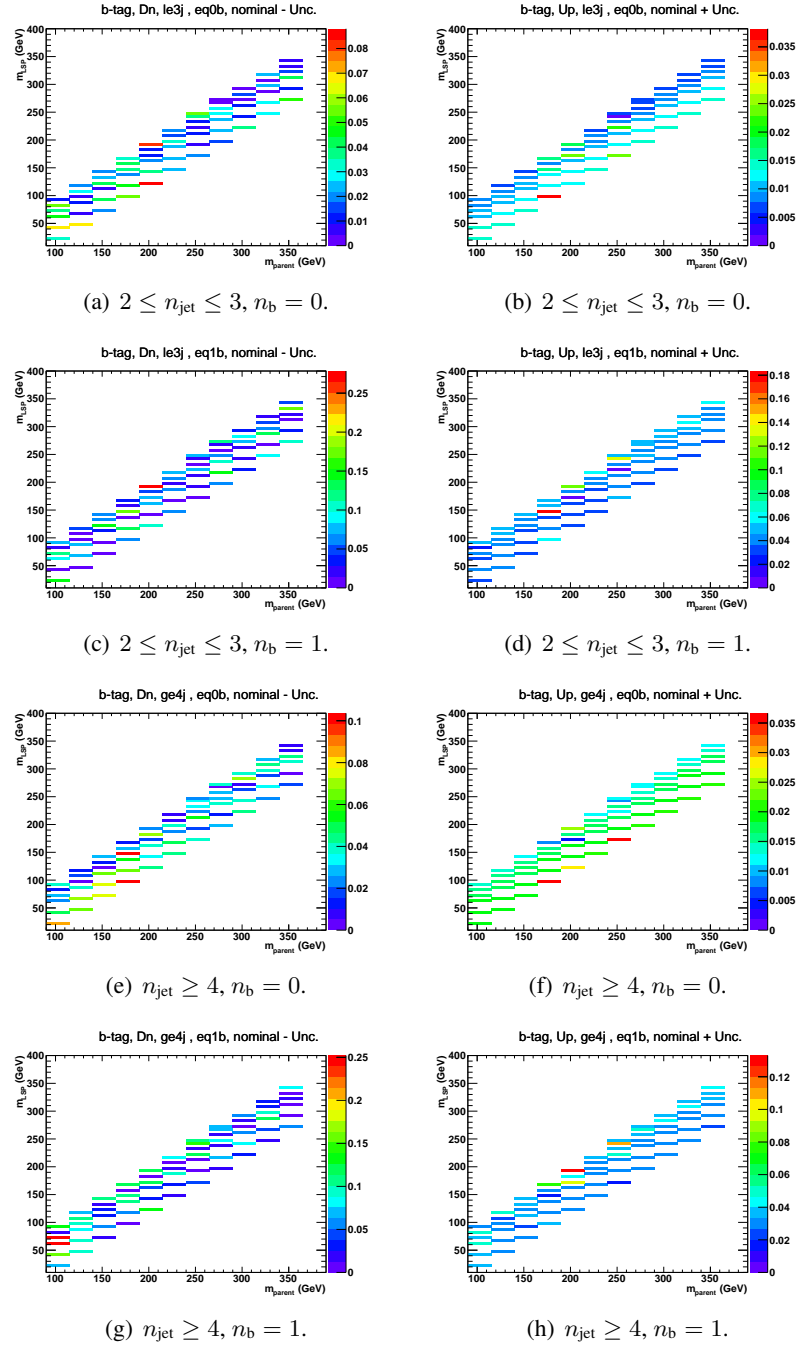


Figure 17: The fractional change in signal efficiency due to systematically (Left) increasing and (Middle) decreasing all b-tag efficiencies according to the scale factor uncertainties, and (Right) the resulting (symmetric) systematic uncertainties due to b-tag scale factor uncertainties for T2cc.

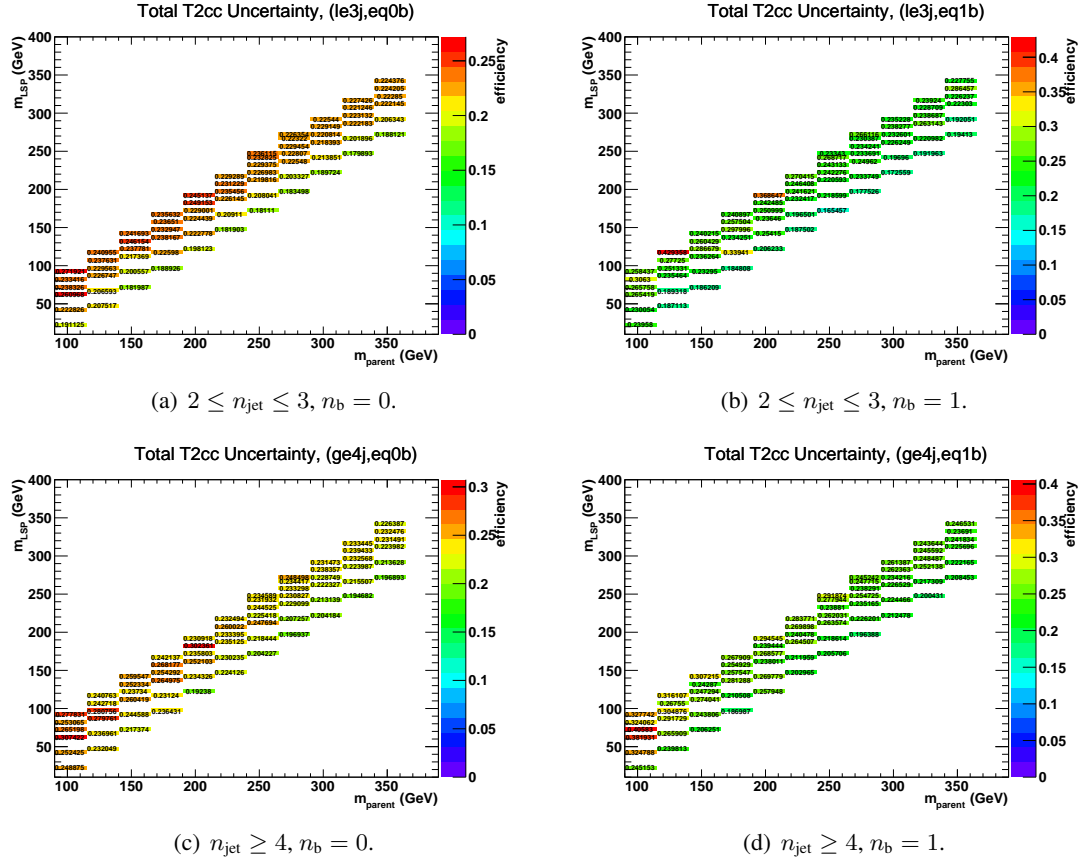


Figure 18: The total systematic uncertainty in the signal efficiency times acceptance for all relevant event categories for the T2cc interpretation.

## C.2 T2tt

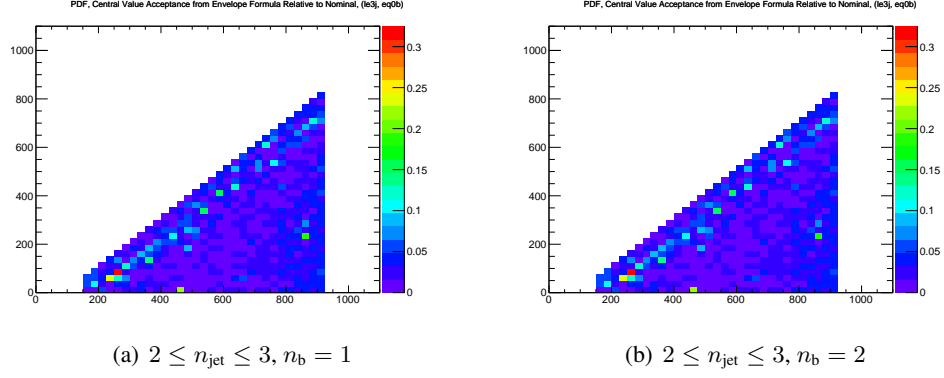


Figure 19: Ratio of efficiency times acceptance for the (middle) central value, (top)  $+1\sigma$  value, (bottom)  $-1\sigma$  value of the envelope calculation relative to the nominal PDF set used to produce the T2tt sample.



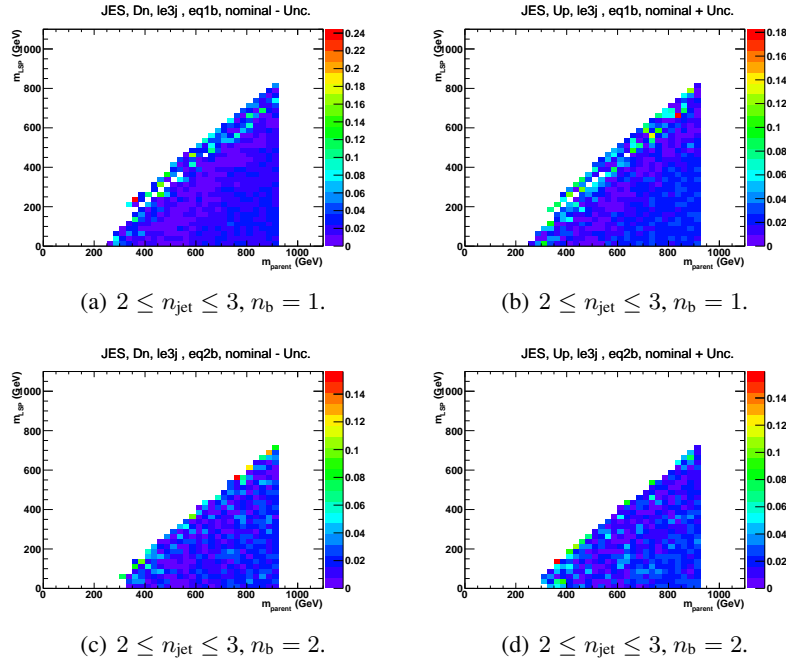


Figure 20: The fractional change in signal efficiency due to systematically (Left) increasing and (Middle) decreasing all jet energies, and (Right) the resulting (symmetric) systematic uncertainties due to JES uncertainties for T2tt.

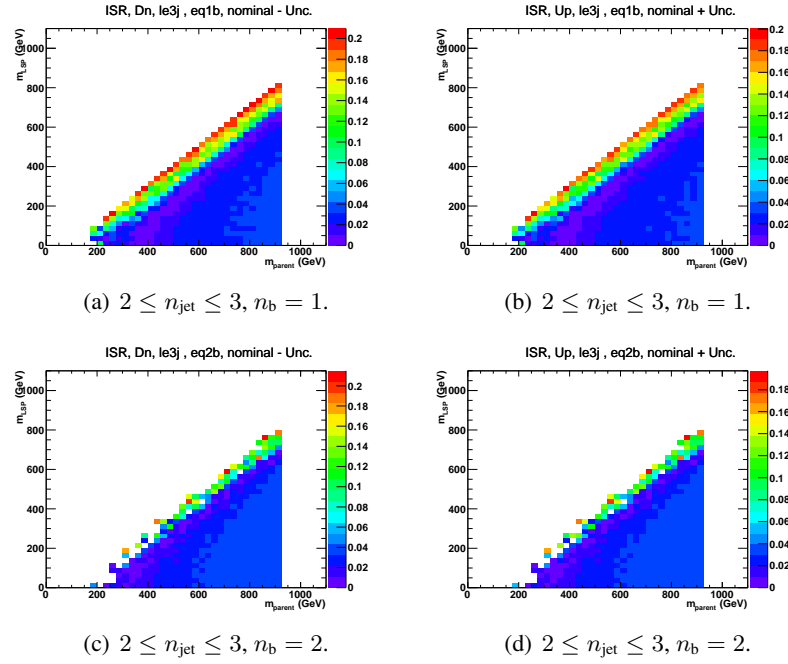


Figure 21: The fractional change in signal efficiency due to systematically (Left) increasing and (Middle) decreasing event weights according to ISR uncertainties, and (Right) the resulting (symmetric) systematic uncertainties due to ISR uncertainties for T2t.

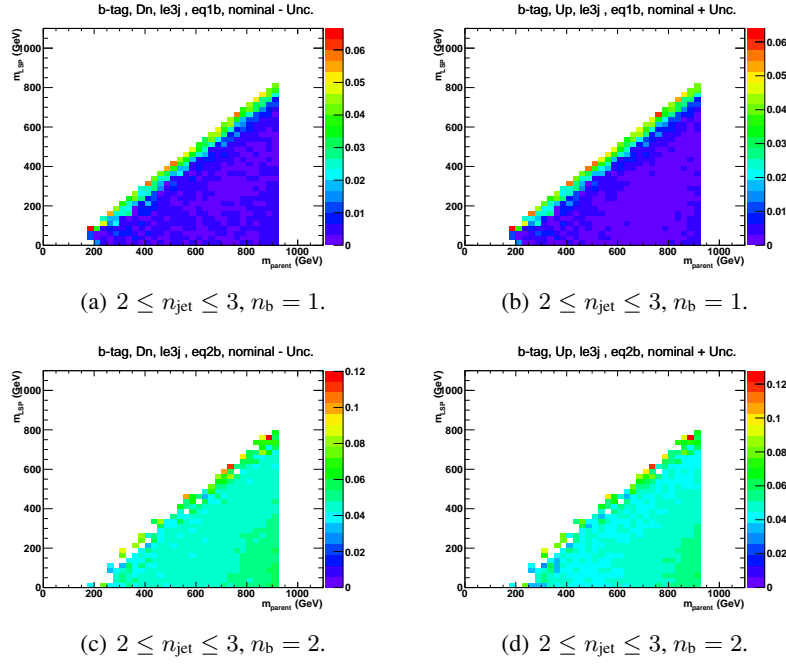


Figure 22: The fractional change in signal efficiency due to systematically (Left) increasing and (Middle) decreasing all b-tag efficiencies according to the scale factor uncertainties, and (Right) the resulting (symmetric) systematic uncertainties due to b-tag scale factor uncertainties for T2tt.

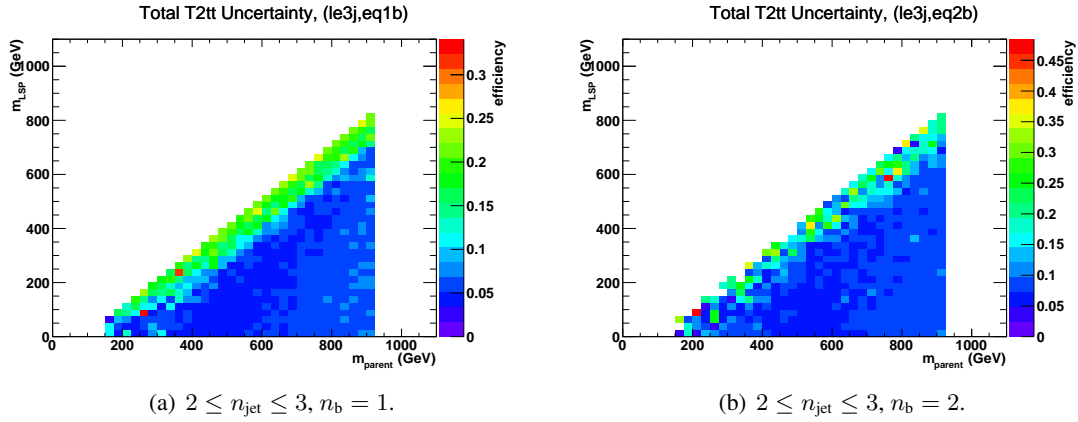


Figure 23: The total systematic uncertainty in the signal efficiency times acceptance for all relevant event categories for the T2tt interpretation.

## References

- [1] D. Alves, N. Arkani-Hamed, S. Arora, et al. Simplified models for lhc new physics searches. 2011. Official summary of results from the 'Topologies for Early LHC Searches' workshop, SLAC, September 2010.
- [2] Johan Alwall et al. MadGraph/MadEvent v4: The New Web Generation. *JHEP*, 09:028, 2007.
- [3] Johan Alwall, My-Phuong Le, Mariangela Lisanti, and Jay G. Wacker. Model-Independent Jets plus Missing Energy Searches. *Phys.Rev.*, D79:015005, 2009.
- [4] Johan Alwall, Philip Schuster, and Natalia Toro. Simplified Models for a First Characterization of New Physics at the LHC. *Phys. Rev.*, D79:075020, 2009.
- [5] M. Botje, J. Butterworth, A. Cooper-Sarkar, et al. The pdf4lhc working group interim recommendations. 2011.
- [6] CMS Collaboration. LO cross sections from the PREP tool. <http://cms.cern.ch/icMS/prep/requestmanagement>.
- [7] CMS Collaboration. Standard Model cross sections at 8 TeV. <https://twiki.cern.ch/twiki/bin/viewauth/CMS/StandardModelCrossSectionsat8TeV>.
- [8] Glen D Cowan. *Statistical data analysis*. Oxford Univ. Press, Oxford, 1998.
- [9] F. James and M. Roos. Minuit: A System for Function Minimization and Analysis of the Parameter Errors and Correlations. *Comput.Phys.Commun.*, 10:343–367, 1975.
- [10] D. Olivito, F. Wurthwein, et al. Hadronic recoil studies of heavy boosted systems, an - 2013/059.

- 
- [11] R. Bainbridge, S. A. Koay. DY+jets at 8TeV: comparison of HT and Njet binned samples.  
<https://indico.cern.ch/event/271369/>.
- [12] Wouter Verkerke and David Kirkby. RooFit. <http://root.cern.ch/drupal/content/roofit>.